UNIVERSITÀ POLITECNICA DELLE MARCHE
Repository ISTITUZIONALE

Inverse methods in aeroacoustic three-dimensional volumetric noise source localization and quantification

(Article begins on next page)

14 January 2025

Corresponding Author: Dr. Gianmarco Battista, PhD

Corresponding Author's Institution: Università Politecnica delle Marche

First Author: Gianmarco Battista, PhD

Order of Authors: Gianmarco Battista, PhD; Paolo Chiariotti, Ph.D.; Milena Martarelli; Paolo Castellini

Abstract: Acoustic source mapping usually involves planar microphone arrays and calculation points located on a surface at a certain distance with respect to the array. An implicit assumption that sources are located on this surface is therefore performed. However, in some application, such as aeroacoustic source identification, this assumption may be wrong and produce misleading results. For this reason, it is interesting to extend the common acoustic mapping techniques to three-dimensional volumetric mapping. Direct beamforming techniques are not suited for volumetric imaging due to poor spatial resolution in radial direction from the array centre. Therefore, more refined algorithms, like deconvolution techniques or inverse methods, are required to obtain intelligible and accurate results. This paper describes the use of inverse methods in the context of aeroacoustic three-dimensional volumetric noise imaging. An Equivalent Source Method is formulated, based on Iteratively Reweighted Least Squares and on Bayesian Regularization. Moreover, a novel approach based on CLEAN-SC as decomposition tool of Cross-Spectral-Matrix in coherent source components is presented.
The method proposed is applied on an aircraft model in wind tunnel. Performance are preliminary assessed with simulated test cases. A comparative investigation in exploiting a single planar array or multiple planar arrays observing noise sources from different directions is performed.

Cover Letter

Dear Editor in Chief,

by this cover letter we would like to invite you to consider the paper *Inverse methods in aeroacoustic three-dimensional volumetric noise source localization and quantification* by Battista, Chiariotti, Martarelli and Castellini for publication in *Journal of Sound and Vibration*.

Acoustic mapping techniques, such as beamforming, are generally used to obtain a map on a plane or surface that represents the object of interest. This entails the assumption that all sources are confined in the chosen surface. However, this assumption may not be true in some application, such as aeroacoustic ones. This work aims at showing how to exploit inverse methods to produce acoustic maps of volumes. The issues of volumetric problems are identified and strategies to cope with them are described. The study compares also the use of a single planar array with the use of two planar arrays combined. The techniques proposed are tested on simulated experiments and then applied on experimental data of an aircraft model in a wind tunnel.

This work is the improvement of the work presented at the International Conference on Noise and Vibration Engineering - ISMA 2018 describing an application on an aircraft model in wind tunnel:

http://past.isma-isaac.be/downloads/isma2018/proceedings/Contribution_610_proceeding_3.pdf

Please would you consider to address the correspondence to Gianmarco Battista, the corresponding author of the work. You can find his contact details listed hereafter:
g.battista@univpm.it
Via Brecce Bianche ,60131, Ancona,

Looking forward to hearing from you, we would like to wish our best regards.

Gianmarco Battista
Paolo Chiariotti
Milena Martarelli
Paolo Castellini

Inverse methods in aeroacoustic three-dimensional volumetric noise source localization and quantification

G. Battista[a,*], P. Chiariotti[a], M. Martarelli[a], P. Castellini[a]

[a]*Università Politecnica delle Marche Via Brecce Bianche 12,60131, Ancona, Italy*

Abstract

Acoustic source mapping usually involves planar microphone arrays and calculation points located on a surface at a certain distance with respect to the array. An implicit assumption that sources are located on this surface is therefore performed. However, in some application, such as aeroacoustic source identification, this assumption may be wrong and produce misleading results. For this reason, it is interesting to extend the common acoustic mapping techniques to three-dimensional volumetric mapping. Direct beamforming techniques are not suited for volumetric imaging due to poor spatial resolution in radial direction from the array centre. Therefore, more refined algorithms, like deconvolution techniques or inverse methods, are required to obtain intelligible and accurate results.

This paper describes the use of inverse methods in the context of aeroacoustic three-dimensional volumetric noise imaging. An Equivalent Source Method is formulated, based on Iteratively Reweighted Least Squares and on Bayesian Regularization. Moreover, a novel approach based on CLEAN-SC as decomposition tool of Cross-Spectral-Matrix in coherent source compo-

---

[*]Corresponding author
Email address: `g.battista@univpm.it` (G. Battista)

nents is presented.

The method proposed is applied on an aircraft model in wind tunnel. Performance are preliminary assessed with simulated test cases. A comparative investigation in exploiting a single planar array or multiple planar arrays observing noise sources from different directions is performed.

Keywords:

---

1. Introduction

Aeroacoustic measurements are usually performed using phased-microphone array techniques to ease the noise source identification and quantification tasks. A general review of acoustic mapping techniques based is available in [1]. The most common configuration is to define the Region Of Interest (ROI) as a plane representing the object and calculate the map on it. This entails the implicit assumption that all noise sources are located on this plane. However, in several applications this is may not be true, especially in aeroacoustic ones. Some approaches in literature consider a three-dimensional surface that adheres to the object, therefore, considering also different source array distances [2, 3, 4]. However, the hypothesis of sources confined in a surface still must be fulfilled to not produce misleading maps. The aim of this paper is to analyse the problem of volumetric acoustic mapping, thus removing this hypothesis, and formulate a method that addresses all the issues arising in this challenging context. Aeroacoustic source mapping will gain the major benefit from this approach.

Literature provides some studies on this kind of applications. Despite

their simplicity and robustness, simple beamforming algorithms, like Conventional Beamforming (CB), suffer of poor dynamics and poor spatial resolution, which lead to difficult interpretation of maps, especially when dealing with volumetric imaging. Therefore, more refined techniques must be adopted. Over the years, deconvolution techniques (e.g. DAMAS [5], CLEAN-SC [6]) of beamforming maps have been developed in order to improve result accuracy in terms of spatial resolution and quantification of source strengths. The goal of these methods is to remove the effect of array spatial response, i.e. the Point Spread Function (PSF), from the map and return the real source distribution that has generated the original map and hence pressure data measured at microphone locations. Deconvolution of CB maps is needed to achieve useful results as explained by Sarradj in [7], where CLEAN-SC is chosen due to its low computational cost and applicability to problems of large size. Instead, an attempt in using DAMAS for three-dimensional applications is provided in [8]. Porteus et al. [9] discussed the need to compensate different source-array distances to avoid a bias of source levels on the map. Padois et al. [10] compared the behaviour of different acoustic mapping methods using one or two planar arrays, showing as a second array on orthogonal plane with respect to the first greatly improves the performance of all imaging methods. In addition, this work focuses the attention also on the computation time of different techniques. In [11], Battista et al. described and compared different inverse methods for three-dimensional acoustic mapping using a single planar array, while Ning et al. [12] adopted compressive sensing techniques with the same purpose.

3

The aim of this paper is to present a novel approach for tackling volumetric acoustic source reconstruction problem. The method proposed grounds on two building blocks.

- CLEAN-SC is used as pre-processing step for extracting coherent source components from array microphone Cross-Spectral Matrix (CSM). Each component can be used as input data in an inverse approach for localizing and quantifying the relevant acoustic sources. Being a coherence based decomposition method it outperforms the standard orthogonal decomposition approach especially when dealing with coherent and spatially distributed aeroacoustic sources.

- Equivalent Source Method (ESM) is used to model the inverse acoustic problem which is then solved through an Iterative Reweighted Least Squares (IRLS) approach specifically tailored to volumetric acoustic source mapping.

The paper is organized as follows: Section 2 introduces the volumetric acoustic source identification problem and the issues related to this topic; Section 3 discusses the IRLS based solver tailored to volumetric mapping; Section 4 provides a detailed description of the CSM decomposition based on CLEAN-SC; Section 5 shows the performance of the approach on simulated and experimental data; Section 6 draws the main conclusions of the work.

4

2. Formulation and analysis of volumetric acoustic source identification problem

2.1. Acoustic direct and inverse problem formulations

In this paper, a frequency domain approach is adopted. Acoustic imaging techniques rely on *Wave Superposition Method* [13], which states that the acoustic field of a complex radiating source can be approximated by a finite number of elementary sources enclosed within the real one. This principle can be adopted to make the source-receiver propagation problem discrete, assuming a set of elementary sources (monopoles, dipoles, plane waves, spherical harmonics, etc.) which can be used to reproduce the actual acoustic field. Therefore, in frequency domain, the discrete acoustic direct problem can be described, for each frequency, by the following linear relationship:

$$\mathbf{Gq} = \mathbf{p} \tag{1}$$

where $\mathbf{q}$ is the vector of complex source strengths of S elementary sources of assumed spatial distribution, $\mathbf{p}$ is the vector containing the complex pressures at M receiver locations and the complex matrix $\mathbf{G}$ represents the discrete acoustic propagator. The calculation of $\mathbf{p}$ for given source coefficients $\mathbf{q}$ and propagator $\mathbf{G}$ is known as *direct acoustic problem*. This is a well-determined problem having a unique solution. Conversely, the calculation of $\mathbf{q}$ for given $\mathbf{G}$ and $\mathbf{p}$ stands for the *inverse acoustic problem*: this is the aim of inverse acoustic imaging techniques. This problem results to be ill-posed in Hadamard sense, i.e. existence, uniqueness and stability of solution are not guaranteed [14]. Also acoustic inverse problems can be expressed as linear

5

transformation

$$\hat{\mathbf{q}} = \mathbf{T}\mathbf{p} \, . \tag{2}$$

The main difference between direct and inverse problem is that, while the direct operator $\mathbf{G}$ is well-defined, the inverse operator $\mathbf{T}$ can assume different forms depending on the approach adopted. For this reason, the estimated source coefficients $\hat{\mathbf{q}}(\mathbf{T})$ depend on how the source field is considered (e.g. assumptions made, a priori information, etc.). A detailed review about different inverse operators is provided by Leclere et al. in [15]. Beamforming techniques consider each potential source singularly, thus having a scalar inverse problem, where the inverse operator is a column. In this case, the inverse operator is known as *steering-vector*. Contrarily, the idea of inverse methods is to take into account all potential sources at once, covering the whole ROI (Region Of Interest) with a set of elementary sources. For this reason, inverse problems are generally under-determined. In fact, the number of microphones (i.e. the number of equations) is limited by practical aspects, while the number of potential sources (i.e. the number of unknowns) is commonly larger. Therefore, in order to define a particular inverse operator, some assumptions on the nature of the source field must be done.

2.2. Analysis of three-dimensional volumetric acoustic inverse problem

The concepts described so far are general and regards any acoustic mapping technique and any kind of ROI (planes, 3D surfaces, volumes, etc.). However, the extension of the spatial domain from surfaces to volumes implicates further considerations. The analysis of volumetric imaging reveals three critical points:

6

P1. potential sources located at very different distances from the array centre;

P2. poor spatial resolution of arrays in radial direction from the array centre;

P3. increase of the number of potential sources with no contribution to the acoustic field.

These issues may affect acoustic imaging techniques in several applications, however, the volumetric approach enhances their effects, therefore, it demands to address all of them properly.

The first one (*P1*) requires balancing energy needed by each potential source to produce the same pressure on microphones, therefore, the different source-receiver distances must be somehow compensated. When this aspect is not considered, imaging approaches based on source field energy minimization would produce biased solutions, systematically penalising the farthest sources. Some applications of the same concept are given in [9, 16].

The second item of the list (*P2*) regards the ability to distinguish sources closely spaced in radial direction. This is critical since variations of the source distance produce very small variations of measured pressure at the array location. Conversely, lateral displacement of a source produces more meaningful variation of amplitude and phase on microphones([7]). The lateral size of the mainlobe is much smaller than the radial size, due to the reasons just explained. Mainly two factors affect the spatial resolution. The first one is

7

the ratio between the array diameter and the wavelength, i.e. the Helmholtz number (He). The second factor is source-array distance. A reduction of the Helmholtz number and/or an increment of the source distance cause the reduction of amplitude and phase difference at microphone. In fact, the higher is the source-array, the more pressure field at microphones is similar to a plane wave (i.e. source at infinite distance). This reduces the sensitivity in retrieving the real source-array distance. This effect is particularly evident when a single planar array is used. However, even when multiple planar arrays are combined together this issue may happen.

The last issue (*P3*) concerns the fact that the size of the region of interest grows. This causes the increment of number of potential sources necessary to cover the ROI but the number of sources to approximate the source field remain almost unaltered. Direct beamformer are affected only by an increment of calculation time, while deconvolution techniques and inverse methods suffer also the increment of unknowns.

3. Sparse approximation of source field with IRLS approach tailored to volumetric mapping

The previous section analyzed those issues related to acoustic imaging that become critical in case of volumetric approach. This paper aims at facing these issues by inverse methods. Indeed, in this section, the algorithm developed by the authors to fulfill this task is presented in a step-by-step mode.

8

3.1. Assumptions on source field

Due to the lack of information in inverse acoustic problems (commonly under-determined), source reconstruction process requires the introduction of some a priori information and making assumptions on source field. Two different hypotheses on the source field are discussed here: *minimum energy source field* and *sparse source field*.

Inverse methods based on minimization of source field energy, i.e. the common Least-Squares (LS) approaches, return maps qualitatively similar to CB, therefore, having poor spatial resolution (*P2*) and poor dynamics. In fact, minimizing the L_2-norm solution causes a split of the energy associated to a real source into several equivalent sources, thus introducing a sort of "blurring" effect [17]. If this kind of results might be satisfying in terms of source localization, the equivalent sources returned by this approach have a directivity pattern towards the array [16], thus producing severely underestimation of the source strength. However, these techniques are useful for the availability of analytic formulae to calculate the solution. In addition, they are related to well-known regularization mechanisms, that are mandatory for inverse problems, such as Tikhonov Regularization (TR) [18] and Bayesian Approach to sound source reconstruction (BA) [19].

Since the assumption of minimum energy source field does not produce satisfying results, the other possible choice discussed here is the hypothesis of *sparse source field*. Real sources can be represented by few non-zero elements in a given representation (monopoles, dipoles, plane waves, spherical

9

harmonics, etc.), as explained in [15]. This can be thought as the research for the simplest combination of elementary sources that matches pressure data measured by the microphones. The choice of the type of elementary sources is equivalent to an a priori assumption on the source field in which sparsity is assumed. Therefore, the more this a priori information corresponds to the reality the more accurate is the sparse approximation of the source field. The assumption of sparsity helps to retrieve correct source strengths and improves localization ability. When dealing with volumetric mapping, sparsity gains much more relevance. In fact, size and shape of real sources do not change, while only the number of potential sources grows (*P3*). Therefore, the need of this hypothesis grows. In addition, the sparsity constraint helps in reducing the lobe-effect (*P2*) experienced with direct beamformers and LS approaches.

As regards the choice of representation basis, only monopoles are adopted in this work. However, the method described hereafter is general enough to consider also different elementary source types.

3.2. Sparsity constraint

Hereinafter, the theory about sparse approximation is briefly provided. Given the direct model of Eq. 1, sparse approximation of the source field can be found minimizing the following cost function:

$$\hat{\mathbf{q}}(\eta^2, p) = \arg\min_{\mathbf{q}} \left(\|\mathbf{G}\mathbf{q} - \mathbf{p}\|_2^2 + \eta^2 \|\mathbf{q}\|_p^p \right) \tag{3}$$

where $\| \cdot \|_p^p$ is the L_p-norm of a vector. The main three terms of this cost function are:

10

- $\|\mathbf{q}\|_p^p$ is the L_p-norm of of the solution, where $0 \leq p \leq 2$. Adjusting the exponent of the norm different sparsity constraint are applied.

- $\|\mathbf{Gq} - \mathbf{p}\|_2^2$ is the fitting error. This term represents the fidelity of the solution with respect to measured data.

- $\eta^2 \geq 0$ is the regularization parameter. This controls controls the trade-off between the two terms above.

The optimization problem in Eq. 3 has no general analytic solution. The only exception is when $p = 2$. In fact, the problem boils down to a regularized LS problem, such as TR or the equivalent case from BA. However, in this case no sparsity is enforced on solution. The measure of sparsity is given by the L_0-norm, often referred to as "pseudo-norm", which counts the number of non-zeros element of a vector. This optimization problem ($p = 0$) is hard to solve exactly, since it is a non-convex optimization problem that can have multiple solutions. However, an approximation of the exact sparse representation can be achieved by using greedy algorithms like (Orthogonal) Matching Pursuit [20, 21]. Due to the difficulty in finding a solution to a non-convex optimization, the problem is reformulated as L_1-norm minimization ($p = 1$), which, under some conditions, returns solutions equivalent to L_0-norm minimization [22]. The advantages are that convex optimization has a unique solution and can be exactly solved using different approaches, such as Basis Pursuit Denoising [23] or the LASSO (Least Absolute Shrinkage and Selection Operator) [24].

A method to approximate the solution of Eq. 3 for $0 \leq p < 2$ arises from

the following consideration:

$$\|\mathbf{q}\|_p^p = \sum_{n=1}^{N} |q_n|^p = \sum_{n=1}^{N} w_{sp,n}^2 |q_n|^2 = \|\mathbf{W}_{sp}\mathbf{q}\|_2^2 \ . \tag{4}$$

This leads to the *Iteratively Reweighted Least Squares* (IRLS) [25] algorithm, which makes use of a diagonal weighting matrix $\mathbf{W}_{sp}$ to converge to a sparse solution solving a Weighted Least-Squares (WLS) problem at each iteration. The idea is to inject a penalty at each iteration to converge to the minimum solution L_p-norm. Weights of the current step depend on the result of the previous iteration, according to the following expression:

$$w_{sp,nn}^{(it)} = \left| \hat{q}_n^{(it-1)} \right|^{\frac{p-2}{2}} \tag{5}$$

where (it) identifies the current iteration and $w_{sp,nn}$ is the *n-th* generic diagonal element. As the exponent of weights is negative for $p < 2$, division by null elements must be somehow avoided to have an invertible weighting matrix. At the first iteration, $\mathbf{W}_{sp}^{(0)} = \mathbf{I}$, thus boiling down to a simple LS problem.

3.3. Weighted Least Squares and Bayesian Regularization

The solution of Weighted Least-Squares problem can be seen as a particular case of a more general approach to inverse problems based on Bayesian inference. In [19], Antoni exploited Bayesian framework for developing a method specific for acoustic inverse problems, which is able to:

- include a priori information on source distribution to better condition the problem and ease the reconstruction task;

- identify the optimal basis functions which minimize the reconstruction error, given the topology of the specific acoustic problem and the a priori information;

- provide a robust regularization criterion.

The core idea of BA is to endow all unknown quantities with a probability density function (pdf) to reflect the lack of knowledge about them. The *likelihood function* encodes measurement errors and describes the direct probability to measure certain pressure values, given the propagation model and the probability density function of measurement noise. Instead, *prior probability density function* reflects the a priori knowledge on source field. A particular solution and regularization mechanism come from maximization of the *posterior probability density function*, thus leading to a *Maximum A Posteriori* (MAP) estimate of source coefficients. When complex normal distribution is assumed for both source coefficients (prior) and noise, the maximization of the posterior probability "mechanically" produces a regularized solution similar to the general form of TR. Otherwise, cost function of Eq. 3 can be derived from BA when a p-generalized normal distribution is assumed as prior pdf [26].

The cost function of a Weighted (Regularized) Least-squares problem is in the following form:

$$\hat{\mathbf{q}}(\eta^2, \mathbf{W}) = \arg\min_{\mathbf{q}} \left(\|\mathbf{G}\mathbf{q} - \mathbf{p}\|_2^2 + \eta^2 \|\mathbf{W}\mathbf{q}\|_2^2 \right) . \qquad (6)$$

The matrix $\mathbf{W}$ is square and invertible. It includes a priori information on source coefficients in the form of its covariance. In this work only diagonal

matrices are used, meaning that the sources are assumed uncorrelated. In this case the inverse operator is calculated as:

$$\mathbf{T} = \mathbf{W}^{-1}(\mathbf{G}\mathbf{W}^{-1})^{+\eta} = \mathbf{W}^{-2}\mathbf{G}^{H}(\mathbf{G}\mathbf{W}^{-2}\mathbf{G}^{H} + \eta^2\mathbf{I})^{-1} \tag{7}$$

where the notation $(\cdot)^{+\eta}$ stands for regularized pseudo-inverse with the regularization parameter η^2. The estimation of this value is equivalent to the determination of the amount of regularization. This is a challenging task since it depends on data, but also on the specific problem and a priori information included with $\mathbf{W}$. Tikhonov Regularization does not provide an internal method for this, but was often used in combination with different criteria to estimate η^2, such as L-curve or Generalized Cross-Validation [27]. However, these methods suffer the presence of multiple local minima, that may bring to random fails in the regularization task, thus having no general automatic and reliable criterion. Bayesian Approach to acoustic source reconstruction explicitly identifies the regularization parameter as the Noise-to-Signal Ratio (NSR), i.e. as the ratio between noise energy and source field energy. Bayesian inference can be exploited also for the estimation of η^2 directly from data, problem formulation and a priori information. Bayesian Regularization (BR) provides different cost functions to fulfil this task, having several advantages with respect to other regularization criteria [28]. The most important is the presence of unique global minimum under some conditions that are generally fulfilled in common applications. The criterion used in this work is the MAP estimate of regularization parameter, selecting the value with maximum probability of occurrence, given the measurements. The definition of the cost function requires the Singular Value Decomposition of

14

$\mathbf{GW}^{-1} = \mathbf{USV}^H$:

$$\mathbf{J}_{MAP}(\eta^2) = \sum_{k=1}^{M} \ln(s_k^2 + \eta^2) + (M - 2)\ln\left(\frac{1}{M}\sum_{k=1}^{M}\frac{|y_k|^2}{s_k^2 + \eta^2}\right) \qquad (8)$$

where s_k are the singular values of $\mathbf{GW}^{-1}$, while the terms $y_k = \mathbf{u}_k^H\mathbf{p}$ are the Fourier coefficients, calculated from the columns of $\mathbf{U}$ and the pressure data $\mathbf{p}$. The minimization of $\mathbf{J}_{MAP}$ with respect to η^2 returns the MAP estimate

$$\eta_{MAP}^2 = \arg\min_{\eta^2}\ \mathbf{J}_{MAP}(\eta^2)\,. \qquad (9)$$

Other cost functions can be obtained from Bayesian framework allowing to include a priori information of noise energy and/or source field energy.

3.4. IRLS tailored to volumetric acoustic mapping

This section describes the IRLS-based method used in this paper to calculate sparse approximation of source fields for volumetric mapping purposes. The algorithm makes use of fixed-point formulation for Eq. 3 which converges to a minimum of the cost function. The minimum is surely global for convex problems ($p \geq 1$), but it may be global or local for non-convex problems ($0 \leq p < 1$). The Bayesian interpretation of IRLS is an Expectation-Maximization algorithm which converges to a MAP solution [29].

The fixed-point scheme can be expressed as:

$$\hat{\mathbf{q}}^{(it)} = F\left(\hat{\mathbf{q}}^{(it-1)}, \mathbf{W}^{(it)}, \eta^{2\,(it)}, \mathbf{G}^{(it)}, \mathbf{p}, p\right)\,, \qquad (10)$$

where the function F is given by Eq. 7. The following procedure is used:

15

1. Set the weighting diagonal matrix for the current iteration as

$$\mathbf{W}^{(it)} = \frac{\mathbf{W}_0}{\|\mathbf{W}_0\|_\infty} \cdot \frac{\mathbf{W}_{sp}^{(it)}}{\|\mathbf{W}_{sp}^{(it)}\|_\infty} \qquad (11)$$

where the diagonal elements of $\mathbf{W}_{sp}^{(it)}$ are calculated using Eq. 5.

2. Estimate the regularization parameter $\eta^{2\,(it)}$ for the current iteration using Eq. 9.

3. Calculate the solution $\hat{\mathbf{q}}^{(it)}$ with the inverse operator of Eq. 7, updated at current iteration.

4. Apply a threshold to discard potential sources that do not contribute significantly to the acoustic field. The set of indices n of potential sources to discard is found using the following criterion:

$$\left\{ n : 10 \log_{10} \left(\frac{|\hat{q}_n|^{(it)}}{\|\hat{\mathbf{q}}^{(it)}\|_\infty} \right) < THR_{dB} \right\} . \qquad (12)$$

The value of THR_{dB} must be negative to keep the most energetic sources. The guidelines on how to properly set this value are provided further on the paper. Discarded sources are set to zero in the final map and correspondent columns of $\mathbf{G}^{(it)}$ are removed.

5. Evaluate a convergence criterion; if not fulfilled go back to step 1, otherwise stop the iterative procedure.

This is the procedure adopted to obtain a sparse approximation of source field. Hereinafter, a discussion about the most important aspects is provided.

Balance of energy among potential sources. Since the first step is always a LS solution, the issue of balancing the energy among potential sources

16

(P1) must be taken into account. Two strategies can be adopted with this purpose. The first one has been described in [16]. The common strength-to-pressure (Q2P) acoustic propagator can be adopted in combination with a weighting strategy. In case of monopoles as potential sources, we have:

$$G_{mn} = \frac{\mathrm{e}^{-\mathrm{j}kr_{mn}}}{4\pi r_{mn}} \quad , \quad w_{nn} = \frac{1}{r_{0n}} \tag{13}$$

where k is the wavenumber. The terms r_{mn} represent the propagation distances between microphones and the potential sources. The terms r_{0n} are the propagation distances between the reference point "0" and the location of potential sources. The reference point (indicated further on with $\mathbf{r_0}$) can be chosen arbitrarily, avoiding the coincidence with a potential source location. The weighting matrix for this correction is diagonal as the others adopted in this paper. The elements of weighted propagation matrix $\mathbf{G}\mathbf{W}^{-1}$ becomes:

$$G_{mn}w_{nn}^{-1} = \frac{r_{0n}}{r_{mn}}\frac{\mathrm{e}^{-\mathrm{j}kr_{mn}}}{4\pi} \ . \tag{14}$$

This weighting strategy must be adopted in addition to any other a priori information introduced in $\mathbf{W}_0$ and $\mathbf{W}_{sp}^{(it)}$. The other approach to balance the energy among potential sources consists of adopting a pressure-to-pressure (P2P) propagator to define the direct operator $\mathbf{G}$. For monopoles, the propagator is in the following form:

$$G_{mn} = \frac{r_{0n}}{r_{mn}}\mathrm{e}^{-\mathrm{j}k(r_{mn}-r_{0n})} \ . \tag{15}$$

This propagator relates the pressure in the reference point "0", generated by a monopole located in n, with the pressure induced on microphone m. Solutions returned by the two formulations of propagator are expressed in

17

different physical quantities (volume acceleration for Q2P and pressure induced in the reference point for P2P). Despite of this, they are equivalent in terms of solution of inverse problem when expressed in the same unit. However, the P2P formulation is adopted in this work to avoid adopting further weighting strategies.

Sparsity constraint. The norm exponent can be set in the range $0 \leq p \leq 2$ to adjust the strength of sparsity constraint. As already reported before, $p = 2$ means no sparsity. In this case, the calculation needs no iterations since the solution is exact. In the range $1 < p < 2$, weak sparsity is enforced and the minimization process still gains advantage in spreading energy of a single source over several potential sources. Convergence is fast and spatial resolution and dynamics are slightly improved. Conversely, in the range $0 \leq p < 1$, strong sparsity constraint is imposed. The norm minimization gains advantage in squeezing the total energy of source field in few equivalent sources. The convergence is faster when p tends to 0, however, it is slower than $1 < p < 2$, since it generally requires more iterations. The advantages of this sparsity constraint are huge in terms of spatial resolution and dynamics. However, some drawbacks may occur. For instance, the representation of spatially extended source may be split into a certain number of non-contiguous equivalent sources. The value $p = 1$ recovers the maximum sparse approximation attainable with convex optimization. It stands for a neutral condition that tends to preserve the real source shape and results are satisfying also in terms of dynamics. This is the case with slowest convergence. Sparse approximation of real source field with equivalent monopoles

18

have some drawbacks in localization. In fact, when spatial resolution of grid of potential monopoles is fine enough, the maximum error in source localization is limited to half grid step. Instead, when the grid is coarse, it may happen that a source is mapped on more than one equivalent source. In this case, the real source location is somewhere in between the equivalent sources.

Discarding strategy of potential sources. After the calculation of solution at current iteration, discarding of potential sources is performed. This step has two reasons: avoid division by zero when weights of $\mathbf{W}_{sp}^{(it)}$ are calculated and speed up the calculation reducing the system size, i.e. the columns of $\mathbf{G}^{(it)}$. The value of THR_{dB} adopted in this work is -100 dB as suggested in [30]. This value has been verified to not affect the results in almost any condition. In fact, higher values may produce the early discarding of sources, that affect the source quantification, leading to underestimation of source strengths.

Convergence criterion. The convergence criterion has a crucial importance in iterative methods, since it guarantees uniformity of convergence in any condition (number and characteristics of real sources, frequency, noise, p, etc.). The one adopted here was derived by [30] and improved by Battista et al. in [11]:

$$MSR = \left\langle \left| \hat{q}_n^{(it)}/\hat{q}_n^{(it-1)} \right| \right\rangle$$
$$\varepsilon^{(it)} = 10 \log_{10} \left(MSR^{(it)} - \left| \Delta(MSR)^{(it)} \right| - \left| \Delta^2(MSR)^{(it)} \right| \right) \tag{16}$$

where MSR stands for *Mean Source Ratio*, the operator $\langle \cdot \rangle$ refers to the

19

spatial average and the operators $\Delta(\cdot)$ and $\Delta^2(\cdot)$ are the backwards finite differences of first and second order respectively. This criterion can be evaluated only for $it > 2$ (given the second order finite difference) and requires solution variation to be small over three last iterations. The algorithm stops when $\varepsilon^{(it)} \geq -0.1$ dB.

A priori information on source distribution. Usually, the experimenter has some a priori information on source locations. Even though this information is vague, the introduction in the calculation process improves the localization and quantification task. Indeed, an example of vague a priori information is the fact that the sources are less likely close to edges of the calculation volume. More reliable information can be retrieved, for instance, from CB maps, similarly to [31]. All knowledge of this kind can be included in $\mathbf{W}_0$. In this algorithm, the choice of reintroducing $\mathbf{W}_0$ in each iteration is made. This is not strictly necessary (and actually represents an arbitrary choice) since after the first iteration, this information would be embedded in $\mathbf{W}_{sp}^{(it)}$. However, it has been experienced that this may help in reducing the risk of artefacts in the map.

3.5. Example of ESM-IRLS volumetric application

The last part of this section is dedicated to an application example of the algorithm just described. Since it is an inverse method, the results strongly depend on several factors, such as array shape, ROI and its discretization, background noise level and others. Therefore, this part should not to be intended as a comprehensive study on the behaviour of ESM-IRLS, but just an example to get more familiar with this technique. The simulated setup

20

consists of a monopole emitting white noise at 1 m distance from the array plane. The ROI is a cube of 1 m on each dimension as depicted in Fig. 1(a). This volume is discretized with a regular grid of monopoles of 2 cm step, thus having 132651 potential sources. The frequency of analysis used for the following examples is 2816 Hz, corresponding to an Helmholtz number $He = 8$. The CB map depicted in Fig. 1(b) is obtained with the steering vector formulation IV described in [7], that is the same adopted throughout the paper for CB. This formulation gives the correct source location at cost of a small error on source level. Commonly, acoustic maps returned by inverse methods are depicted as source strength (volume velocity or acceleration). A different choice is made here because this is the direct output of ESM-IRLS since P2P formulation is adopted for $\mathbf{G}$. In fact, acoustic maps in this paper show the pressure induced by each source at the reference point $(20 \log_{10}(p/p_{ref})$ with $p_{ref} = 20 \ \mu\mathrm{Pa})$.
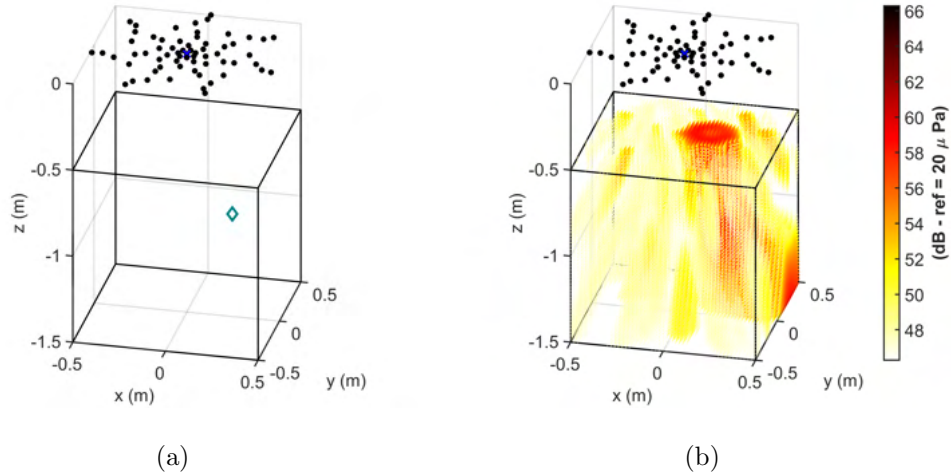
Figure 1: Example of volumetric mapping. (a) Simulated setup, (b) CB map.

21

Two aspects are discussed here: the choice of sparsity constraint and the choice of the reference point. As regard the amount of sparsity constraint, Fig. 2 depicts the results obtained with three values. The map returned from L_2-norm minimization is qualitatively similar to a CB map. Instead, the results achieved with strong sparsity constraint are the ones desired in volumetric imaging. When p is set equals to 1, the monopole is mapped into very few equivalent sources, while $p = 0$ makes it possible to reconstruct the actual source field. In this case, the hypothesis of sparsity perfectly matches with actual source field, therefore, the condition is ideal.
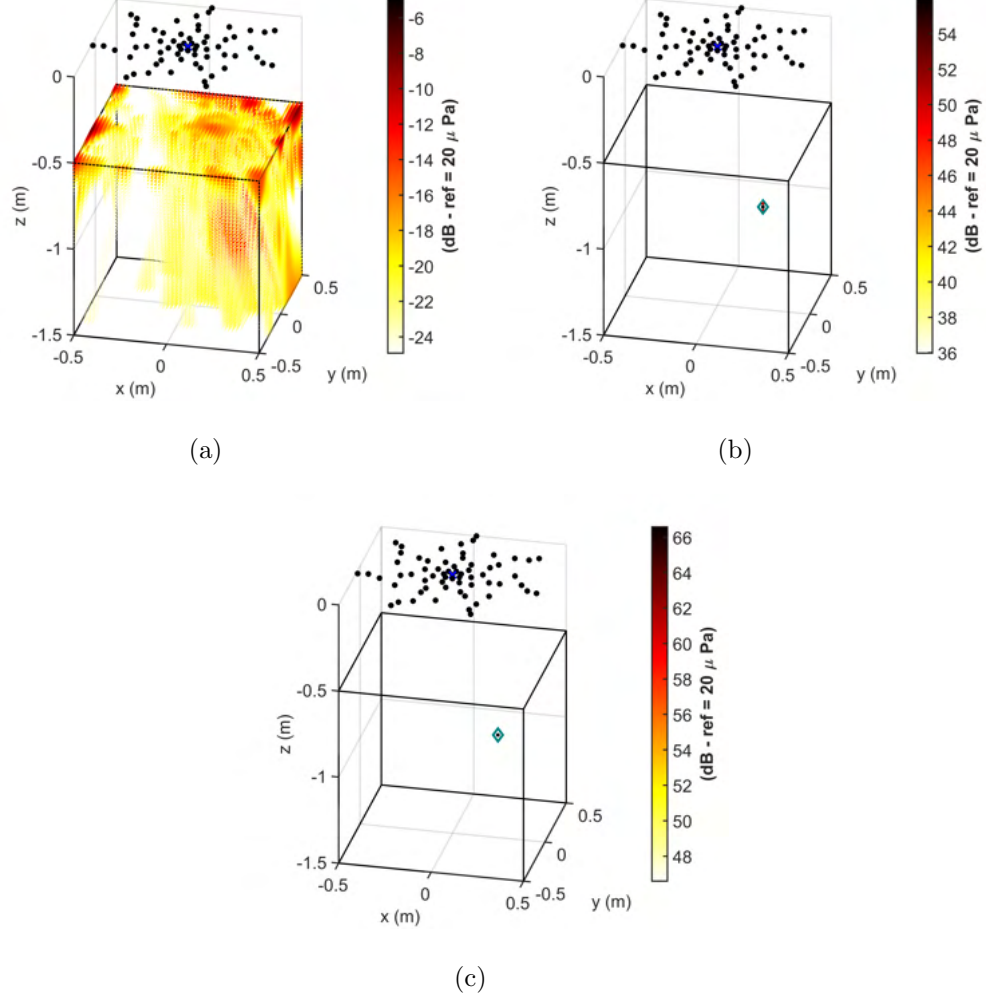
Figure 2: Example of volumetric mapping. ESM-IRLS with different levels of sparsity constraint. (a) $p = 2$, (b) $p = 1$, (c) $p = 0$.

The other important aspect treated here is the choice of the location of the reference point. The maps in Fig. 2 have the reference point at the array centre $\mathbf{r}_0 = \mathbf{0}$. Figures 3 and 4 show the results obtained with different choices. The maps of first IRLS iteration (L_2 minimization) show

artefacts in different positions depending on the reference point. However, the sparse approximation obtained is the same with any $\mathbf{r_0}$. The different level noticeable in Fig. 4 is due to the greater distance between the source and the reference point. It has been experienced that the choice of the reference point does not affect significantly the final map, especially with strong sparsity constraints.

(a)   (b)
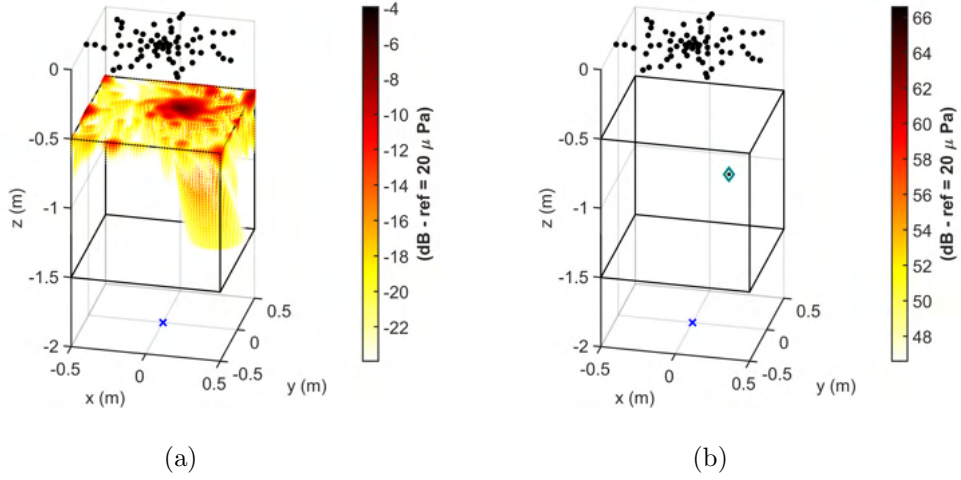
Figure 3: Example of volumetric mapping. ESM-IRLS with reference point in front of the array and on the other side of the ROI w.r.t. the array, $\mathbf{r}_0 = (0, 0, -2)$. (a) $p = 2$, (b) $p = 0$.

24
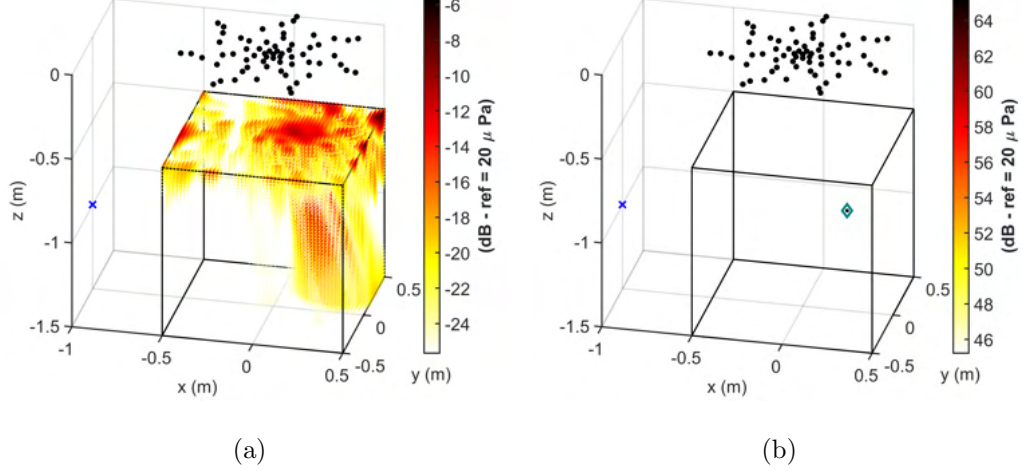
Figure 4: Example of volumetric mapping. ESM-IRLS with reference point laterally to the ROI, $\mathbf{r}_0 = (-1, 0, -1)$. (a) $p = 2$, (b) $p = 0$.

4. Cross-Spectral Matrix decomposition based on CLEAN-SC

The usual input of acoustic imaging techniques in frequency domain is the estimate of Cross-Spectral Matrix $\mathbf{P}$. Many techniques directly handle the full CSM to provide the final map, such as CB and other methods based on it (e.g. DAMAS). Also some inverse methods use the whole CSM, such as sparse acoustical holography based on iterated Bayesian focusing (IBF) [32] and Covariance Matrix Fitting (CMF) [33]. Instead, other imaging methods rely on decomposition of CSM in coherent source components. The problem of source separation has been treated by Dong et al. in [34]. In these cases, the full acoustic map is the sum of single mapped components. The IRLS approach described in the previous section solves the inverse problem in the linear formulation Eq. 1, therefore, pressure data must be in the form of complex pressure $\mathbf{p}$ vector.

25

Techniques like Orthogonal Beamforming [35] or Generalized Inverse Beamforming (GIBF). [17] make use of the Eigenmode Decomposition (ED) of CSM, which is Hermitian and non-negative definite by construction. Given these properties, the CSM can be decomposed as follows

$$\mathbf{P} = \mathbf{E}_{vec}\,\mathbf{E}_{val}\,\mathbf{E}_{vec}^H\,, \tag{17}$$

where $\mathbf{E}_{vec}$ is a unitary square matrix of M orthonormal eigenvectors and $\mathbf{E}_{val}$ is a diagonal matrix containing the corresponding real positive eigenvalues. It is possible to define the eigenmode $\mathbf{e}_i$ as the eigenvector including its amplitude

$$\mathbf{e}_i = \sqrt{e_{val,i}}\,\mathbf{e}_{vec,i} \qquad i = 1,\ldots,M \tag{18}$$

where $\mathbf{e}_{vec,i}$ is the i-th eigenvector and $e_{val,i}$ is the corresponding eigenvalue. Each eigenmode represents a coherent signal across the microphones, under the constraint of orthogonality.

This decomposition is exploited by OB assuming that each eigenmode contains only one coherent point source. In this way, the CB map of each eigenmode has its maximum at the real source location. Then, all peak locations and powers of each partial CB map are added on the full map. When the assumption is verified, the OB final map is the perfect deconvolution of CB map. However, it commonly happens to have different conditions. Firstly, more than one real source component is present in each eigenmode. Secondly, more than one correlated or spatially extended sources may be present. In these cases, the OB map is incomplete in terms of source locations but it is still correct in terms of total power. The complete map of

26

the "content" of each eigenmode can be achieved with GIBF, that defines an inverse problem for each eigenmode:

$$\mathbf{G}\mathbf{q}_i = \mathbf{e}_i \qquad i = 1,\ldots,C \qquad (19)$$

where $C \leq M$ is the number of relevant eigenmodes. Each problem defined in such way is equivalent to the problem of Eq. 1, In this way, each coherent signal is mapped revealing possible multiple coherent sources or spatially extended radiators. Full map is obtained from the energetic sum of solutions obtained from each component $\hat{\mathbf{q}}_i$. A limit of ED, especially when dealing with aeroacoustic measurements, the trend of CSM eigenvalues is typically smooth, thus making difficult to properly set C for each frequency. A possible solution is to map all eigenmodes without checking the relevant ones. Another drawback of ED is that, in real applications, each eigenmode is a mixture of several contributions, therefore, it is not able to achieve a sufficient component separation, except for rare cases.

Another popular acoustic mapping technique, based on CSM decomposition, is the CLEAN based on spatial source coherence (CLEAN-SC) [6]. This deconvolution technique make use of the concept of spatial source coherence explained in [36] to separate source components and build the so called "clean map". Basically, this is a greedy deconvolution algorithm which identifies the maximum on CB map, the so called "dirty map", and extracts the source component that is coherent with the peak, exploiting the fact that side lobes of single source map are spatially coherent with the main lobe. Then the peak is added on the clean map and the CSM is updated subtracting the last component extracted. At this point the new dirty map is calculated and the

27

procedure restarts again. The complete algorithm is reported here:

1. Initialize the clean-map $\mathbf{Q}$ as $S \times 1$ vector, setting all S potential source powers of the ROI equal to 0.

2. Initialize the degraded CSM: $\overline{\mathbf{D}}^{(0)} = \overline{\mathbf{P}}$ (overline stands for removing diagonal elements setting them to zero).

3. Begin the new iteration calculating the CB map (the so called "dirty map") using the degraded CSM of previous iteration $\overline{\mathbf{D}}^{(it-1)}$.

4. Find the maximum peak location on the current dirty map. Identify the source power $P_{max}^{(it-1)}$ and the steering-vector $\mathbf{w}_{max}^{(it)}$ associated to the peak.

5. Calculate the single coherent source component $\mathbf{h}^{(it)}$ solving the following equation

$$\mathbf{h}^{(it)} = \frac{1}{\left(1 + \mathbf{w}_{max}^{H\,(it)}\,\mathbf{H}^{(it)}\,\mathbf{w}_{max}^{(it)}\right)^{1/2}} \left(\frac{\overline{\mathbf{D}}^{(it-1)}\mathbf{w}_{max}^{(it)}}{P_{max}^{(it-1)}} + \mathbf{H}^{(it)}\mathbf{w}_{max}^{(it)}\right) ,$$

(20)

where $\mathbf{H}^{(it)}$ contains the diagonal elements of $\mathbf{h}^{(it)}\mathbf{h}^{H\,(it)}$. This is an implicit expression that can be solved iteratively staring with $\mathbf{h}^{(it)} = \mathbf{w}_{max}^{(it)}$.

6. Update the degraded CSM:

$$\overline{\mathbf{D}}^{(it)} = \overline{\mathbf{D}}^{(it-1)} - \varphi P_{max}^{(it-1)}\mathbf{h}^{(it)}\mathbf{h}^{H\,(it)} ,$$

(21)

where the parameter $0 < \varphi \leq 1$ is the loop-gain.

7. Update the clean-map:

$$Q_s = Q_s + \varphi P_{max}^{(it-1)} ,$$

(22)

where s is the source index where $P_{max}^{(it-1)}$ is detected.

28

8. Go back to step 3 and iterate until the following stop criterion is not satisfied

$$\|\overline{\mathbf{D}}^{(it)}\|_1 \geq \|\overline{\mathbf{D}}^{(it-1)}\|_1 . \tag{23}$$

The clean map obtained in this way represents the deconvolution of the CB map. The spatial source coherence adopted by CLEAN-SC in source component separation outperforms the assumption of orthogonality adopted in ED. This technique is widely used in aeroacoustic applications due to its capability of achieving high accuracy and dynamics. This method is also suitable for volumetric mapping due to the good accuracy and low computational cost [37, 10]. However, some drawbacks must be taken into accounts. In case of close sources the peak location in the dirty map is somewhere in between actual source locations, therefore the extracted component is a combination of these sources. Then the residual energy of these is extracted in the components of following iterations. This behaviour has been improved in a newer version of the method, i.e. High Resolution CLEAN-SC [38]. Similarly to OB, multiple coherent sources or extended coherent radiators are mapped as a single point source. This is due to the fact that only the information of peaks $P_{max}^{(it-1)}$ in CB maps are transferred to the clean map. This drawback is partially mitigated from the use of a loop gain $\varphi < 1$ that splits a coherent component in more than one. Despite of this, the optimal value of φ depends on the application. Lastly, the accuracy in retrieving correct source location is strictly linked to CB.

29

4.1. CLEAN-SC Decomposition procedure

Given the overview above on how to handle the CSM. A novel approach presented in this paper makes use of CLEAN-SC as a tool to extract coherent source components from CSM. As mentioned above, a loss of spatial information happens in standard CLEAN-SC when distributed and/or coherent sources are present. In these cases, phase difference and relative amplitude information of coherent/distributed sources are actually contained in $\mathbf{h}^{(it)}$, but they are not exploited except for CSM degradation. The original idea presented here is to use all informations extracted to build coherent source components $\mathbf{c}_i$ similarly to eigenmodes

$$\mathbf{c}_i = \sqrt{P_{max}^{(i-1)}}\,\mathbf{h}^{(i)} \qquad i = 1, \dots, IT \tag{24}$$

where IT is the number of iterations for each frequency. The CSM decomposition procedure described below is named here CLEAN-SC Decomposition (CSCD) to differentiate it from the original deconvolution algorithm. This simplified procedure considers $\varphi = 1$ to minimize the number of extracted components and the calculation of clean-map is avoided since it is not needed for decomposition purposes. Similarly to GIBF, an inverse problem can be set and solved for each component

$$\mathbf{G}\mathbf{q}_i = \mathbf{c}_i \qquad i = 1, \dots, C \tag{25}$$

One advantage of this decomposition is that the number of relevant components C for each frequency is directly given by the number of iterations IT, which corresponds to the number of components extracted. The full map is obtained, also in this case, from the energetic sum of all contributes.

30

The steps of CSCD are reported here:

1. Initialize the degraded CSM: $\overline{\mathbf{D}}^{(0)} = \overline{\mathbf{P}}$.

2. Begin the new iteration calculating the dirty map using the degraded CSM of previous iteration $\overline{\mathbf{D}}^{(it-1)}$.

3. Find the maximum peak location of the current dirty map. Identify the source power $P_{max}^{(it-1)}$ and the steering-vector $\mathbf{w}_{max}^{(it)}$ associated to the peak.

4. Calculate the single coherent source component $\mathbf{h}^{(it)}$ solving the following equation

$$\mathbf{h}^{(it)} = \frac{1}{\left(1 + \mathbf{w}_{max}^{H\,(it)}\,\mathbf{H}^{(it)}\,\mathbf{w}_{max}^{(it)}\right)^{1/2}} \left(\frac{\overline{\mathbf{D}}^{(it-1)}\mathbf{w}_{max}^{(it)}}{P_{max}^{(it-1)}} + \mathbf{H}^{(it)}\mathbf{w}_{max}^{(it)}\right)\,, \tag{26}$$

where $\mathbf{H}^{(it)}$ contains the diagonal elements of $\mathbf{h}^{(it)}\mathbf{h}^{H\,(it)}$. This implicit expression can be solved iteratively staring with $\mathbf{h}^{(it)} = \mathbf{w}_{max}^{(it)}$.

5. Update the degraded CSM

$$\overline{\mathbf{D}}^{(it)} = \overline{\mathbf{D}}^{(it-1)} - P_{max}^{(it-1)}\mathbf{h}^{(it)}\mathbf{h}^{H\,(it)}. \tag{27}$$

6. Go back to step 2 and iterate until the following stop criterion is not satisfied

$$\|\overline{\mathbf{D}}^{(it)}\|_1 \geq \|\overline{\mathbf{D}}^{(it-1)}\|_1\,. \tag{28}$$

These are the steps needed for CSM decomposition. It is worth noticing that it is possible to use also lower values for φ, however, the number of components increases, thus requiring more computation to solve inverse problems.

31

4.2. Difference between deconvolution with CLEAN-SC and imaging with CLEAN-SC decomposition

Results on a simple simulated experiment are provided to highlight the issues of deconvolution with CLEAN-SC and the advantage in using CSCD in combination with ESM-IRLS (or other imaging techniques). The same concept is valid for ED and OB. Three monopoles emitting white noise are simulated. Source 1 and 3 are driven with the same signals. Source coordinates and levels are reported in Table 1, while Fig. 5 depicts the array and the CB map. The latter clearly reveals three sources. However, Fig.6 shows that CLEAN-SC misses the third source. This happens because the maximum peak is on source 1 and the component extracted contains whatever is coherent with it. The map obtained with ESM-IRLS correctly shows three monopoles as equivalent sources. Figure 7 shows the CB maps of the first two components extracted via CSCD. Map of first component reveals the source 3 correlated with the strongest one.

	x	y	z	Level
Source 1	0.20	0.20	-1.0	0 dB
Source 2	-0.20	0.10	-1.0	-3 dB
Source 3	0.20	-0.20	-1.0	-6 dB

Table 1: Three monopoles example. Source coordinates (m) and levels (dB). Source 1 produces 1 Pa rms at 1 m distance.

(a)

(b)
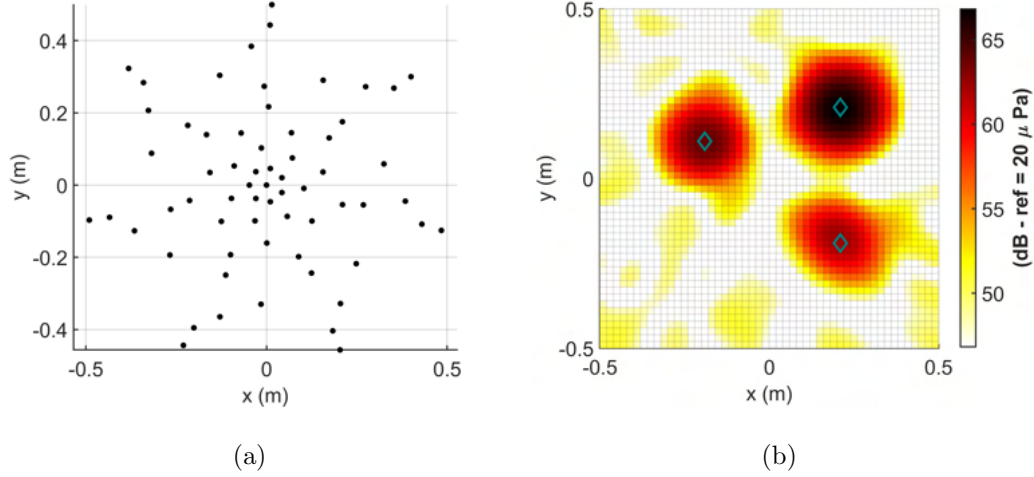
Figure 5: Three monopoles example. (a) 64 microphone array, (b) CB map.

(a)

(b)
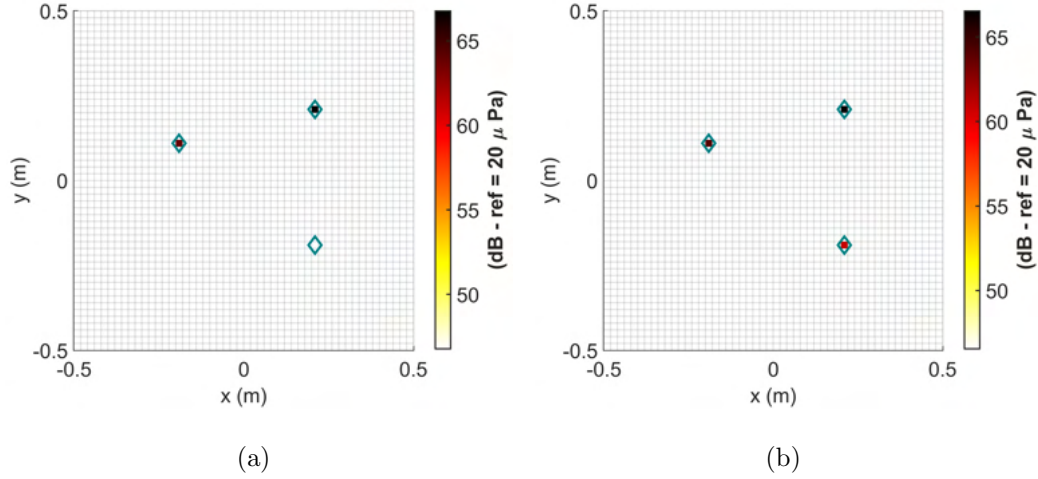
Figure 6: Three monopoles example. Comparison between standard CLEAN-SC and ESM-IRLS with CSCD. (a) CLEAN-SC $\varphi = 0.6$, (b) ESM-IRLS $p = 0$ with CSCD.

33
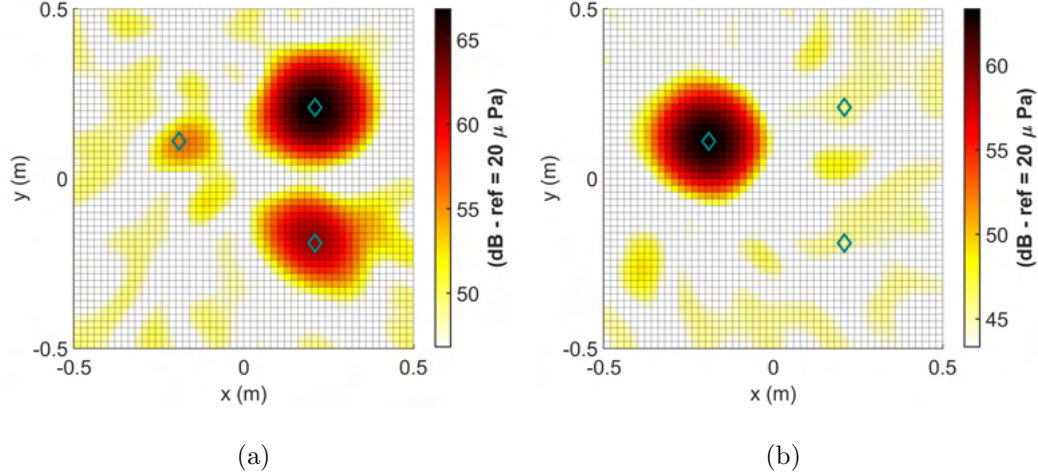
Figure 7: Three monopoles example. CB maps of first two components extracted with CSCD. (a) Component 1, (b) Component 2.

5. Application results

5.1. Reference set-up

The test program was conducted at the Pininfarina Aerodynamic and Aeroacoustic Research Center in Turin, Italy, within the EU WENEMOR project. Pininfarina's facility contains a test section of 8 m × 9.6 m × 4.2 m (see Figure 8(a)). The wind tunnel was specifically acoustically treated in order to reduce reverberation and background noise. Two planar microphone arrays were installed at Pininfarina Wind Tunnel (WT), as depicted in Figure 8(b): a 78 microphone wheel array (3 m diameter) placed at the ceiling of the WT at a distance of 2.5 m from the model axis and a 66 microphone half-wheel array (3 m diameter) located broadside, parallel to the axis of the open rotor and 4.2 m far from the longitudinal axis of the model. Signals were synchronously sampled at a sample rate of 32768 Hz for a total observation

34
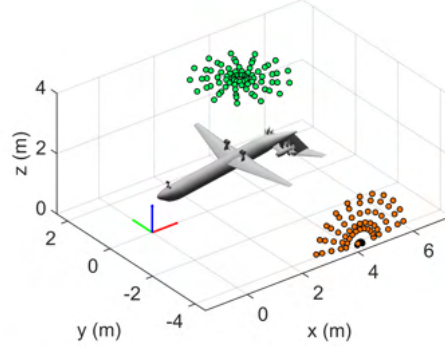
Figure 8: (a) Test set-up in Pininfarina WT (front view of the aircraft model). (b) Microphone array layout with respect to WT and aircraft model (green dots: top wheel array, orange dots: side half-wheel array)

length of 10 s. Time data has been processed to estimate CSM using Welch's method (block size: 1024 samples, overlap: 50%, window: Hanning).

The CROR tested featured two rotors of 12 blades each. Both left and right engines of the aircraft model were driven from a single power supply and controlled by dedicated control systems (one per motor). Strouhal number scaling was performed to represent flight conditions of the full scale aircraft. Different design configurations of the model were tested during the whole test campaign (different tails, rotors in pusher and tractor configuration, different distances of the CRORs with respect to the model fuselage, etc.) at different flow speeds and angles of attack. Angle of attacks (AoA) differed also with respect to the take-off or approach model configuration. However, all the results discussed in this paper refer to the T-tailed model, in approach condition with CRORs in pusher configuration for AoA = 8 deg and flow

speed of 28 m/s. The flow direction is considered to be the X positive axis of the coordinate system represented in Figure 8(b) (red arrow). Assumption of propagation through uniform flow field is done [39]. For this reason, propagation distances are calculated as virtual distances corresponding to the actual travelling time for a given flow field and speed of sound, thus leading to the following expression for r_{mn}:

$$r_{mn} = \frac{\|\mathbf{r}_n - \mathbf{r}_m\|_2}{-C_{mn} + \sqrt{C_{mn}^2 - M_a^2 + 1}} \quad , \quad C_{mn} = (\mathbf{r}_n - \mathbf{r}_m) \cdot \hat{\mathbf{f}} \, M_a \qquad (29)$$

where $\hat{\mathbf{f}}$ is the flow direction and M_a is the Mach number. Both for simulated and experimental cases, the reference point is set at the origin of coordinate system, i.e. $\mathbf{r}_0 = \mathbf{0}$. Equation 29 is also used to calculate terms r_{0n}.

Before analysing the experimental data recorded, some simulated test cases are presented. The aim of simulated data is to better understand performance of methods in terms of source localization, quantification and dynamics achievable. Same frequency range in considered in both simulated and experimental tests, i.e. acoustic maps reported hereinafter refers to one-third octave band at 2500 Hz. In addition, same arrays, ROI and algorithm settings are adopted.

5.2. Simulated data

Each simulated test case consists of four monopoles emitting uncorrelated white noise and located in the four spots depicted in Figure 9. Monopole levels and coordinates are chosen in order to simulate typical sources of noise expected in a real setup. Source 1 is the loudest (1 Pa rms at 1 m distance) and represents the CROR noise, sources 2 and 3 represent the wing tip noise

36

(a)   (b)
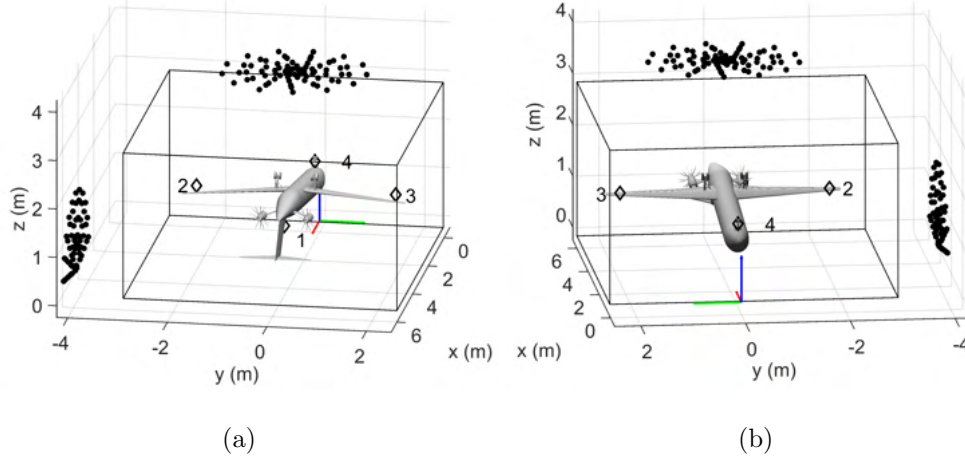
Figure 9: Position of simulated sources (black diamonds) with respect to the aircraft model. The black dots represent microphone locations of the two arrays - (a) Rear view. (b) Front view.

and are 10 dB weaker than source 1, finally, source 4 is positioned on the front landing gear and is 20 dB weaker than source 1. During measurement campaign, time signals of real WT noise were acquired by the arrays without the model in the test section at flow speed of 28 m/s. These signals have been used as background noise (BGN), in the synthesis of simulated signals, to obtain more realistic simulations. The idea of such simulation is to have a background noise with a spatial distribution and not the ideal spatially white noise. In fact, the real BGN produces well-structured artefacts on maps and it may come outer of the ROI considered. What it is not taken into account in these simulations is the sensor calibration uncertainty and phase mismatch. Indeed, these can deteriorate performance of imaging techniques. Some array calibration procedures were developed to reduce the effect of these issues [40, 41]. As regard inverse methods, sensor calibration uncertainty can be

37
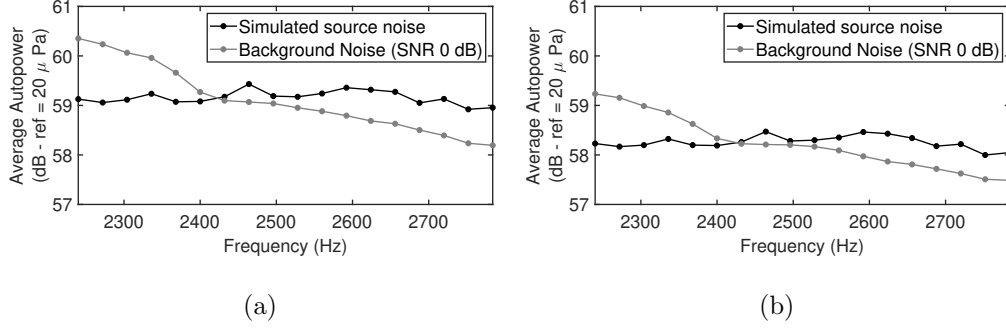
Figure 10: Average microphone auto-spectra - (a) Top array, (b) Side and top arrays

relevant in the amount of regularization, therefore, this problem should be considered when measurements are performed.

Synthetic microphone signals are produced as sample-by-sample sum of two contributions: simulated source signals and recorded BGN. Therefore, simulated total pressure $p_{tot,m}(t)$ on each microphone is obtained as follows

$$p_{tot,m}(t) = p_{sig,m}(t) + G \cdot p_{bgn,m}(t) \qquad m = 1, \ldots, M \qquad (30)$$

where $p_{sig,m}(t)$ is the contribution of all simulated sources on each microphone and $p_{bgn,m}(t)$ is the real WT noise recorded by each m-th microphone. Since the real BGN has not flat spectrum, the value of the gain G must be set to properly scale BGN signals to get the desired Signal-to-Noise Ratio (SNR) in the band of interest. The proper value of G has been calculated using microphone auto-spectra, averaged over all microphones, of both simulated and real WT noise signals. Once selected the frequency band of interest (2500 Hz one-third octave band here), the overall band power P_{sig} and P_{bgn} are estimated and used to calculate G as

$$G = \sqrt{\frac{P_{sig}}{P_{bgn}}} 10^{(-\mathrm{SNR}_{dB}/20)} \qquad (31)$$

38

where SNR_{dB} is the target SNR, expressed in dB. In this way, data produced have the desired overall SNR for the band of interest. Two different test cases are studied in this section: noise-free and SNR 0 dB. Figure 10 shows the average microphone auto-spectrum induced by simulated source noise compared with average microphone auto-spectrum of background noise added for the noisy test case.

The volume of interest, depicted in Figure 9, contains the whole model and it is discretized with a regular grid of monopoles using a step of 0.06 m, thus having 464508 potential sources in the volume. Grid step has been chosen to be less than half wavelength that is approximately 0.138 m for the centre frequency of the band. Maximum sparsity enforced by setting $p = 0$. Both ED and CSCD are used to map noise sources and then compared in terms of localization and robustness to noise. All CSCD components are mapped while the number of relevant eigenmodes is set to $C = 20$. Diagonal removal is not performed with ED since it does not produce any meaningful advantage, while it is adopted with CSCD. Maps obtained with standard CLEAN-SC are reported to make a comparison with ESM-IRLS. In addition, the use of CB map of each component as a priori information $\mathbf{W}_0$ has been evaluated and compared with the results without a priori information. When dual array is used, microphone signals are processed together as it were a unique array. All maps are represented using a dynamic range of 50 dB. As regards source quantification, volume acceleration of reconstructed sources are calculated integrating the maps over a sphere of 0.25 m radius having the centre in the exact source position. Results are depicted as the ratio between

59   39

reconstructed and exact source volume acceleration.

(a)

(b)
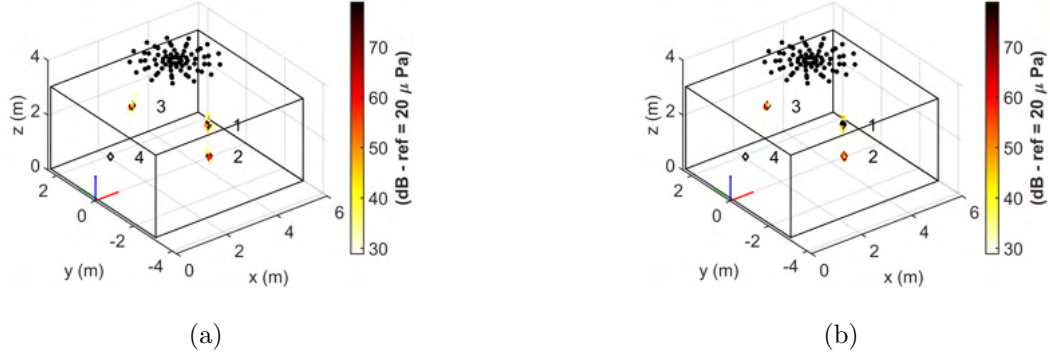
Figure 11: Noise-free simulation. Top array and ESM-IRLS. (a) CSCD, (b) ED.

(a)

(b)
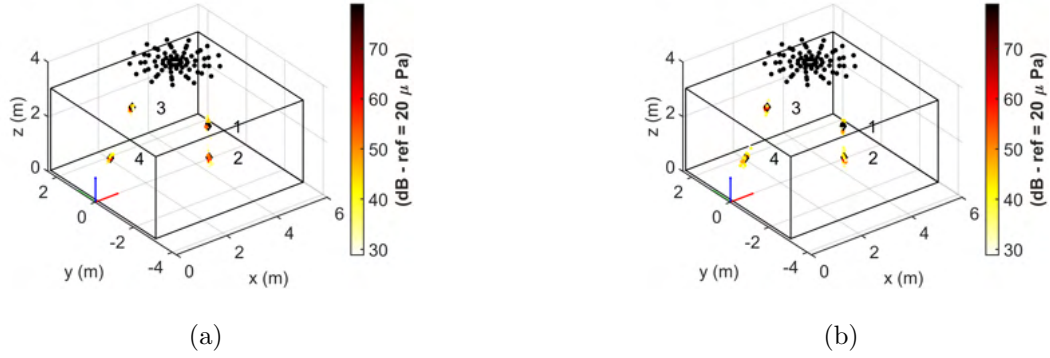
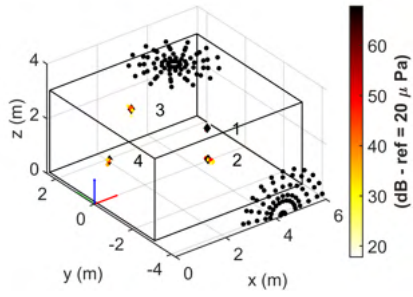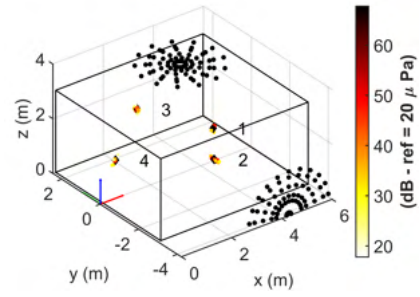Figure 12: Noise-free simulation. Top array and ESM-IRLS with CB map as a priori information. (a) CSCD, (b) ED.
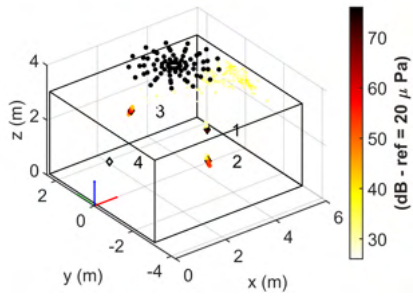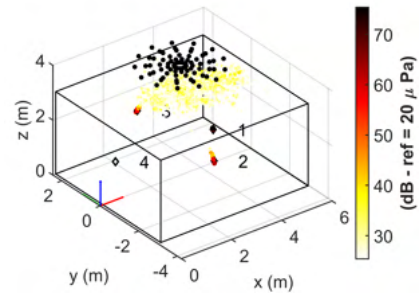
(a)

(b)
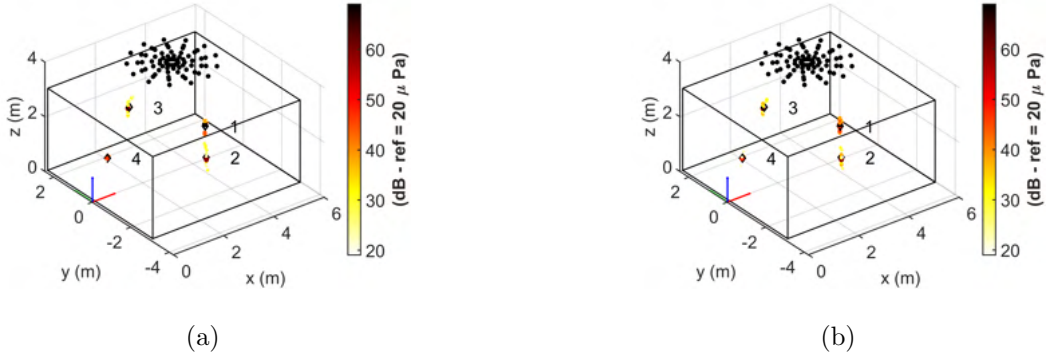
Figure 13: Noise-free simulation. Top array and CLEAN-SC. (a) $\varphi = 1$, (b) $\varphi = 0.6$.

(a)

(b)
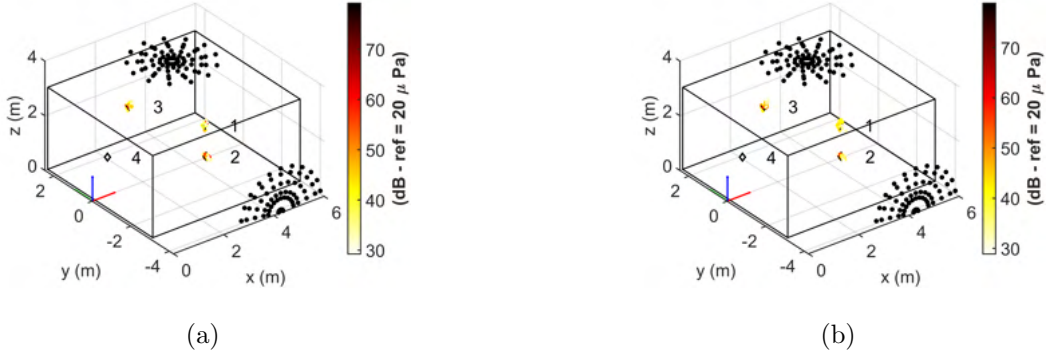
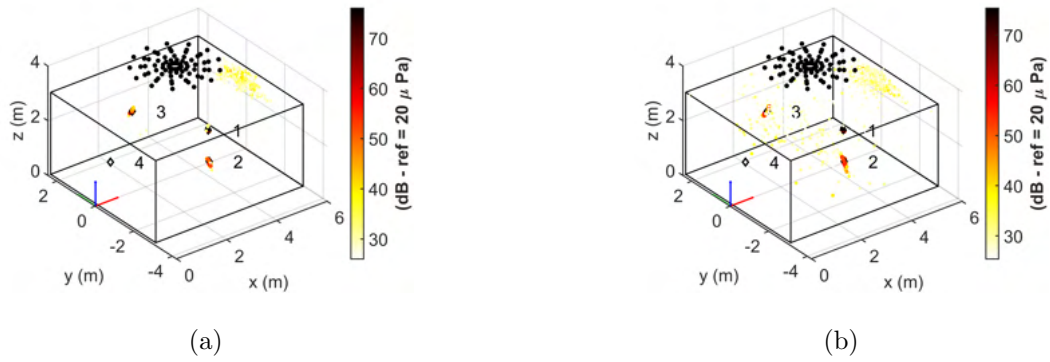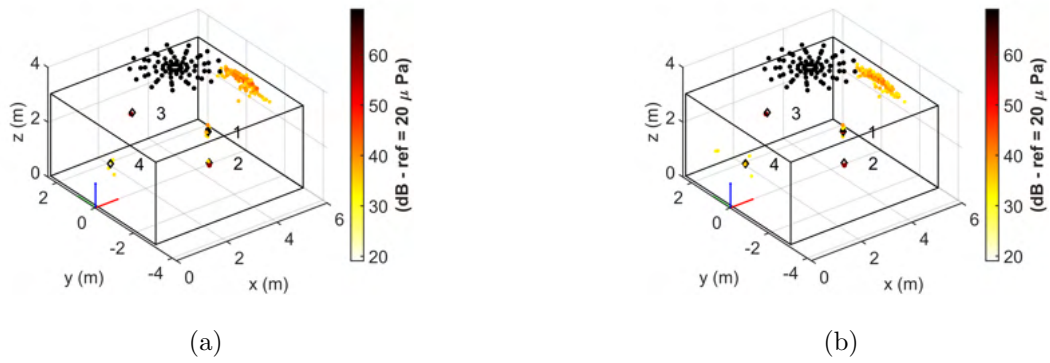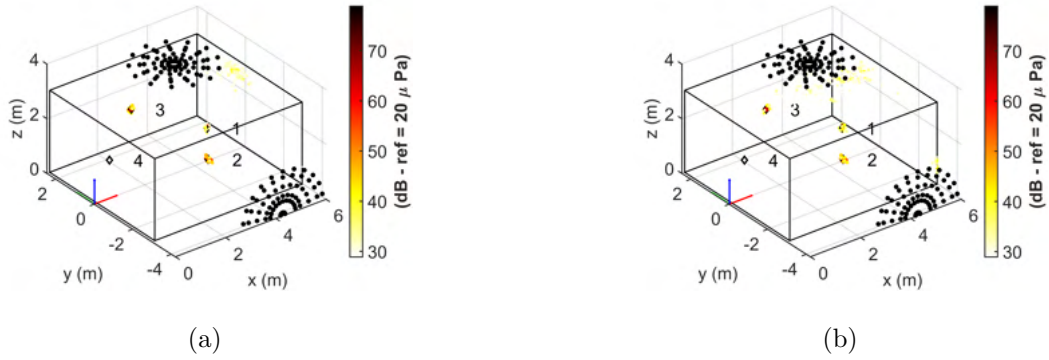Figure 14: Noise-free simulation. Side and top arrays and ESM-IRLS. (a) CSCD, (b) ED.

(a)

(b)
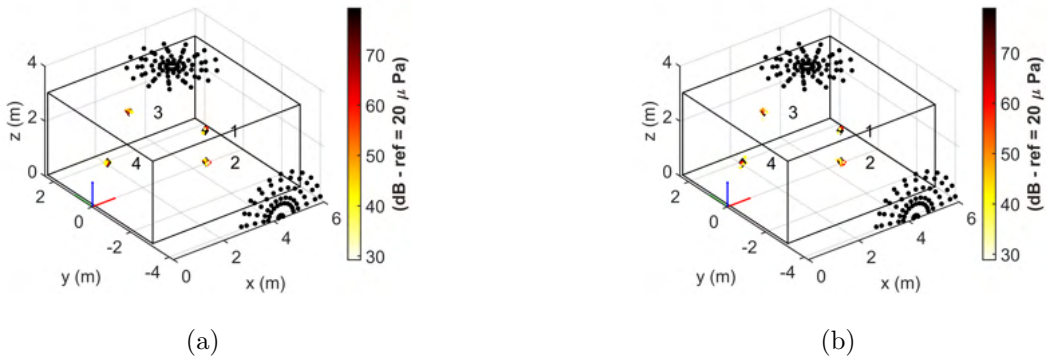
Figure 15: Noise-free simulation. Side and top arrays and ESM-IRLS with CB map as a priori information. (a) CSCD, (b) ED.

41

Figure 16: Noise-free simulation. Side and top arrays and CLEAN-SC. (a) $\varphi = 1$, (b) $\varphi = 0.6$.

Figure 17: Simulation with SNR $= 0$ dB. Top array and ESM-IRLS. (a) CSCD, (b) ED.

Figure 18: Simulation with SNR = 0 dB. Top array and ESM-IRLS with CB map as a priori information. (a) CSCD, (b) ED.

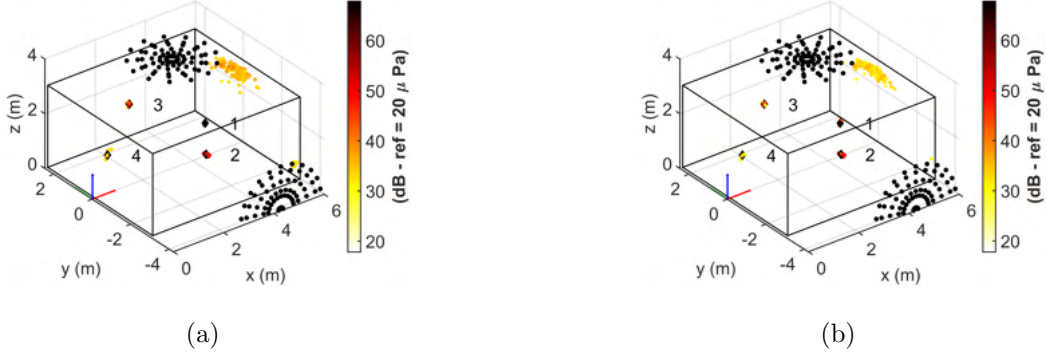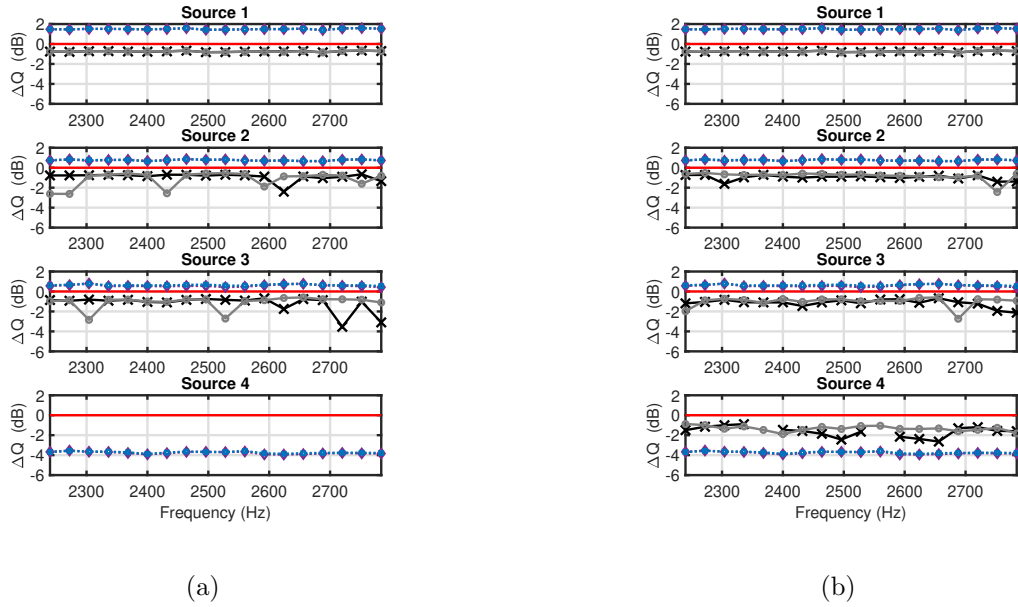Figure 19: Simulation with SNR = 0 dB. Top array and CLEAN-SC. (a) $\varphi = 1$, (b) $\varphi = 0.6$.

(a)   (b)

Figure 20: Simulation with SNR = 0 dB. Side and top arrays and ESM-IRLS. (a) CSCD, (b) ED.

(a)   (b)
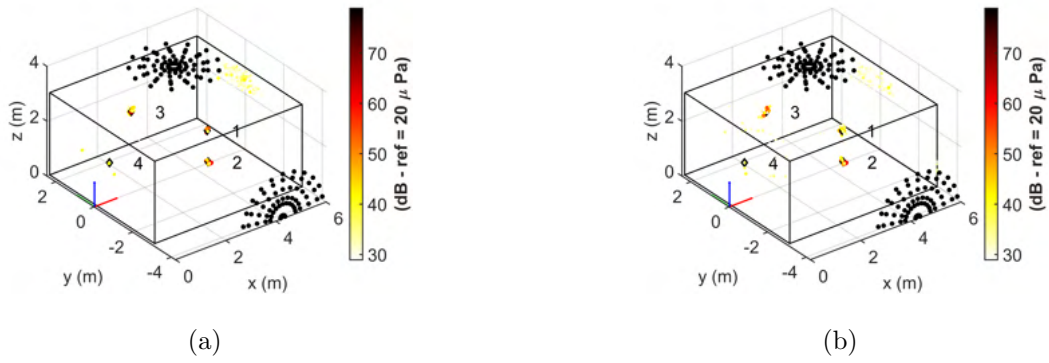
Figure 21: Simulation with SNR = 0 dB. Side and top arrays and ESM-IRLS with CB map as a priori information. (a) CSCD, (b) ED.

(a)　　　　　　　　　　　　　　　　　(b)

Figure 22: Simulation with SNR $= 0$ dB. Side and top arrays and CLEAN-SC. (a) $\varphi = 1$, (b) $\varphi = 0.6$.

(a)　　　　　　　　　　　　　　　　　(b)
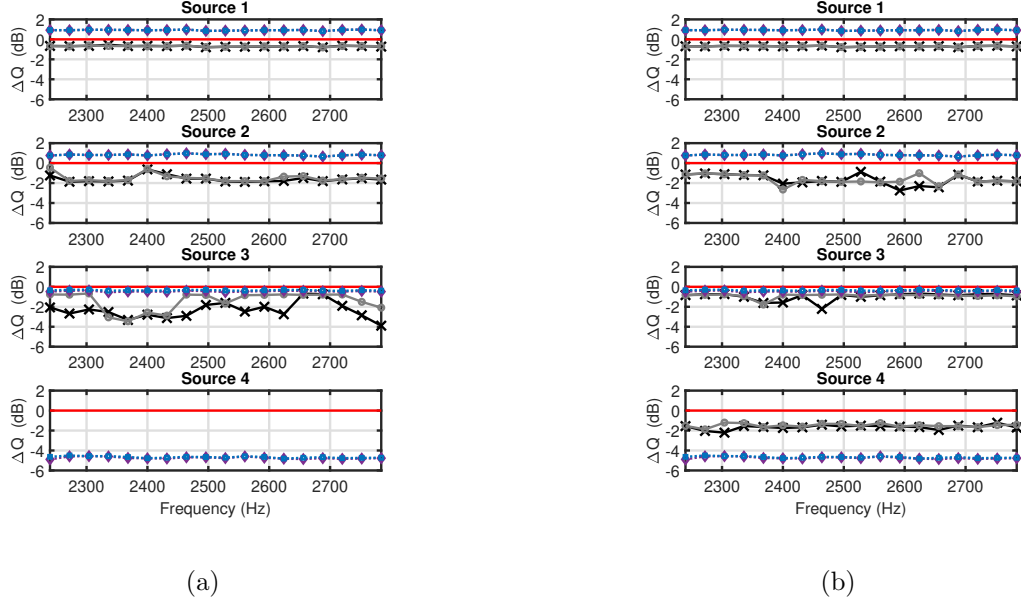
Figure 23: Noise-free simulation. Error of reconstructed source spectra using top array (dB references are the exact source spectra). Solid lines: ESM-IRLS (black crosses: ED, grey circles: CSCD). Dotted lines: CLEAN-SC (blue squares: $\varphi = 0.6$, purple diamonds: $\varphi = 1$). (a) ESM-IRLS without a priori information, (b) ESM-IRLS with CB as a priori information.
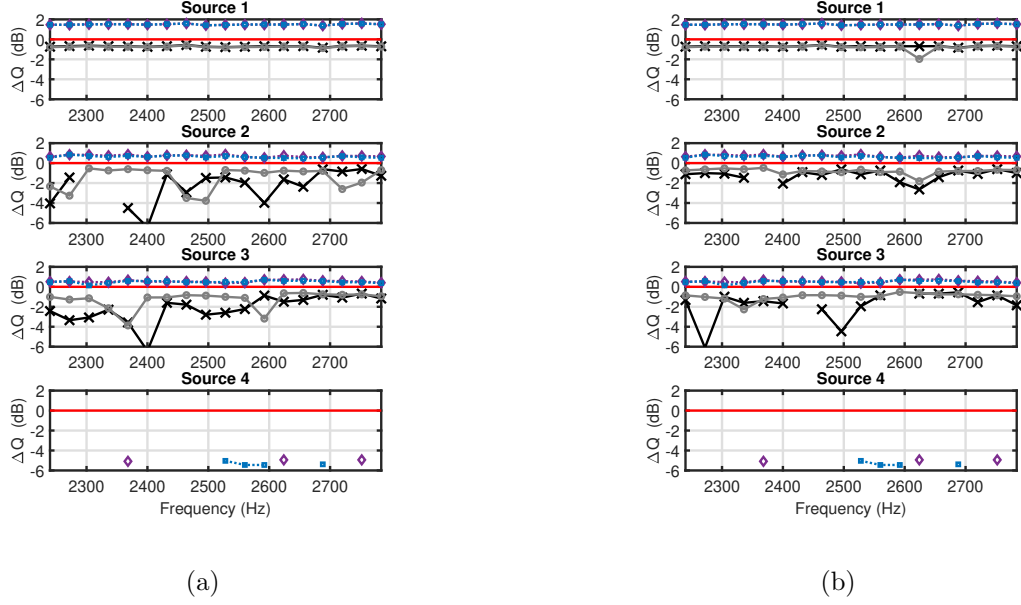
45

(a)   (b)

Figure 24: Noise-free simulation. Error of reconstructed source spectra using side and top arrays (dB references are the exact source spectra). Solid lines: ESM-IRLS (black crosses: ED, grey circles: CSCD). Dotted lines: CLEAN-SC (blue squares: $\varphi = 0.6$, purple diamonds: $\varphi = 1$). (a) ESM-IRLS without a priori information, (b) ESM-IRLS with CB as a priori information.
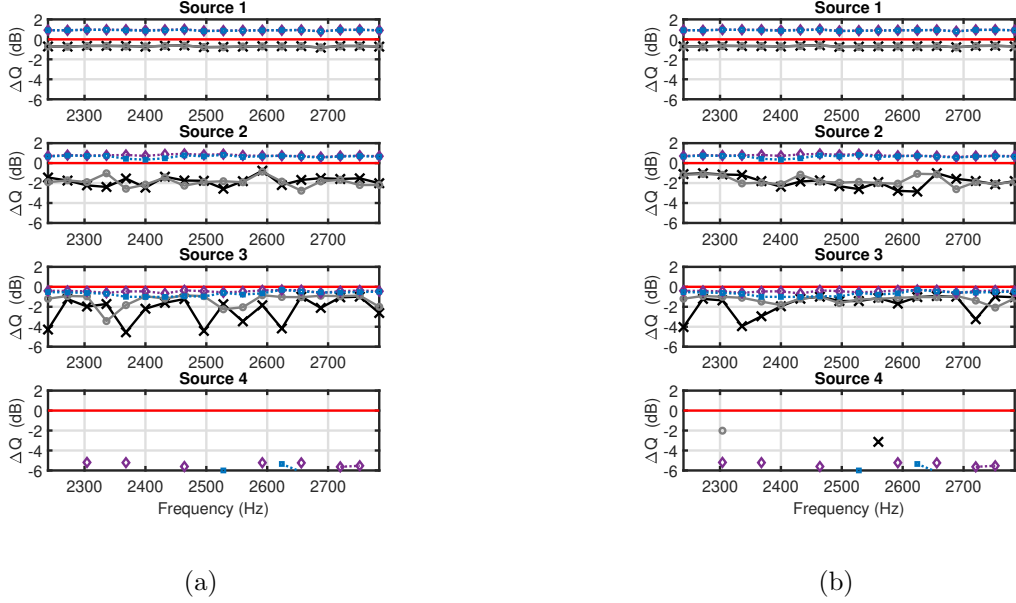
46

(a)

(b)

Figure 25: Simulation with SNR = 0 dB. Error of reconstructed source spectra using top array (dB references are the exact source spectra). Solid lines: ESM-IRLS (black crosses: ED, grey circles: CSCD). Dotted lines: CLEAN-SC (blue squares: $\varphi = 0.6$, purple diamonds: $\varphi = 1$). (a) ESM-IRLS without a priori information, (b) ESM-IRLS with CB as a priori information.

(a) (b)

Figure 26: Simulation with SNR = 0 dB. Error of reconstructed source spectra using side and top arrays (dB references are the exact source spectra). Solid lines: ESM-IRLS (black crosses: ED, grey circles: CSCD). Dotted lines: CLEAN-SC (blue squares: $\varphi = 0.6$, purple diamonds: $\varphi = 1$). (a) ESM-IRLS without a priori information, (b) ESM-IRLS with CB as a priori information.

These results show how it is possible to properly produce volumetric mapping, even in case of strong background noise (Figures from 11 to 16). Noise-free case shows that ESM-IRLS does not reveal the weakest source (20 dB below the loudest), unless a priori information are provided. This happens independently from the use of single or dual array. Conversely, CLEAN-SC always reveals the weakest source without BGN. As regard quantification of sources, Figures 23 and 24 shows that both methods are able to recover the source strength with an error of about 2 dB. Generally, CLEAN-SC overestimates source level, except for the weakest source that is underestimated of 4

dB. Instead, ESM-IRLS always produces an underestimation of about 0.5 dB for the strongest source and a a bit higher for the others. The introduction of a priori information with CB of each component makes more stable the quantification and enables the estimation of the weakest source strength. In this case, any meaningful difference is noticeable between ED and CSCD.

Test case with background noise (Figures from 17 to 22) shows that volumetric imaging is feasible also in this severe condition. The first three sources are detected in almost all conditions (array and algorithm). Instead, the weakest source is revealed only by CLEAN-SC. In all maps, the wind tunnel noise is visible on the top left part of the volume. This is due to fan noise coming outside the ROI. It is worth noticing to further analyze Fig. 17. In this case, ESM-IRLS is combined with ED, where only the top array is used and no a priori information is included. These hard conditions makes that the source reconstruction process fail, thus producing a solution where great part of the energy is concentrated in the layers of potential sources near the array. In similar conditions, this phenomenon does not occur when CSCD is utilized, due to better separation of source signal from noise. Even with a priori information, ED returns worse map than CSCD. In fact, more random artefacts are present in the map and sources 2 and 3 are not well concentrated at the right source-array distance but they are blurred along the radial direction from the array centre. Results of source quantification remains the same only for the strongest source. Instead, reconstructed spectra of sources 2 and 3 suffer of major instability with ESM-IRLS especially without a priori information and only top array is used, while CLEAN-SC

49

has much more stable behaviour in this case.

Therefore, both quantification and localization gain benefit from the injection of a priori information in calculation, resulting in more stable and better addressed problem. The use of a second array is particularly useful in presence of background noise, as it increases localization accuracy and the capability of suppressing noise and artefacts. Reconstructed source spectra with CLEAN-SC are almost independent from φ in this application.

5.3. Experimental data

Experimental data were acquired both with CRORs turned-on and turned-off. An estimate of SNR in both test conditions can be retrieved using the average microphone auto-power spectrum (Fig. 27). When rotors are functioning, the difference of band power between test condition and WT background noise is about 15 dB. Instead, when rotors are not running, the difference shrinks to 8 dB. In the band of interest In the band of interest also an harmonic of CROR rotation speed is present (approximately 2624 Hz).

Even the experimental test are mapped with ESM-IRLS (combined with CSCD and ED) and CLEAN-SC. The number of relevant eigenmodes was empirically set to $C = 20$ because otherwise the noise spoils excessively the CSM eigenmodes. The maximum number of CSCD components was limited to 20, but it results a lower number for all spectral lines in the band of analysis. Diagonal removal is not performed with ED since it does not produce any meaningful advantage even in this noisy environment, while it is adopted with CSCD. The volume of interest is the same of the simulated

50

test case. Two values of loop gain are adopted for CLEAN-SC ($\varphi = 1$ and $\varphi = 0.6$). Figures from 28 to 33 show the result of acoustic mapping on the test case with the CRORs switched-on. Figures from 34 to 39 show the acoustic maps with the CRORs switched-off.
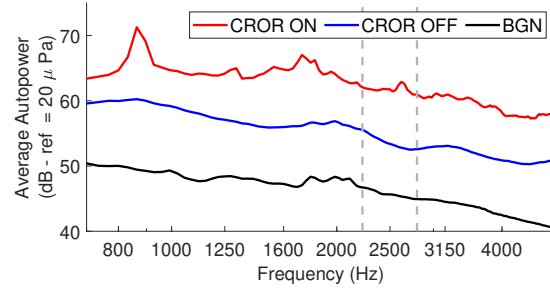

Figure 27: Average microphone spectra of three test condition: CRORs switched-on (red line), CRORs switched-off (blue line) and background noise (black line). Vertical dashed lines represent the band analyzed in this paper.
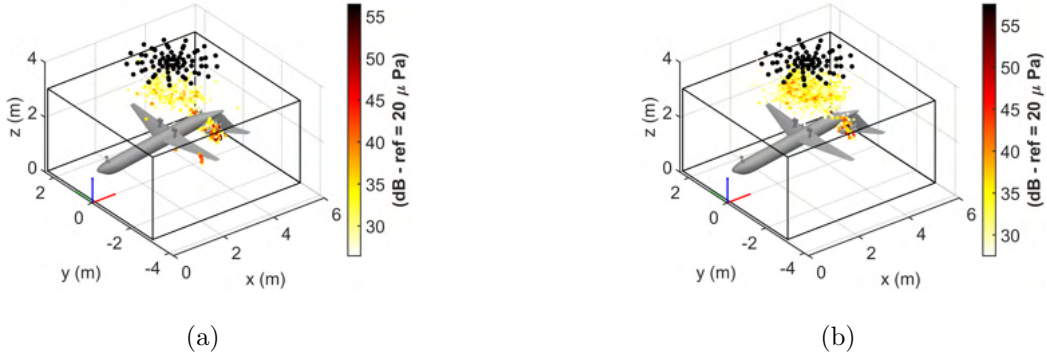

(a)

(b)

Figure 28: CROR turned-on. Top array and ESM-IRLS. (a) CSCD, (b) ED.

51

(a)

(b)
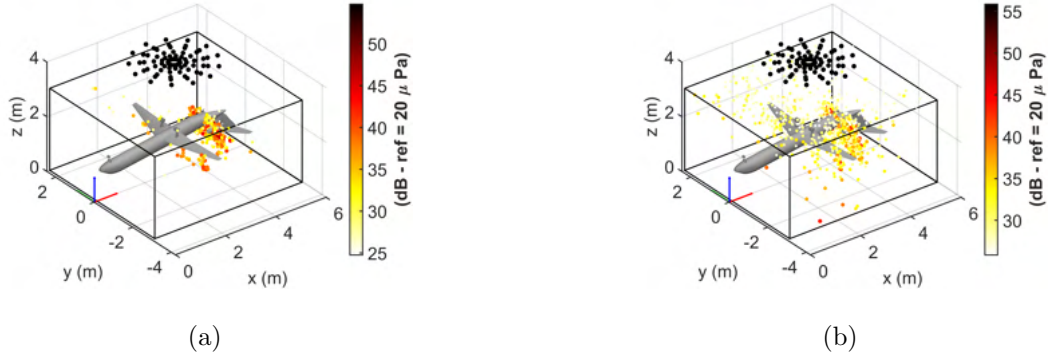
Figure 29: CROR turned-on. Top array and ESM-IRLS with CB map as a priori information. (a) CSCD, (b) ED.
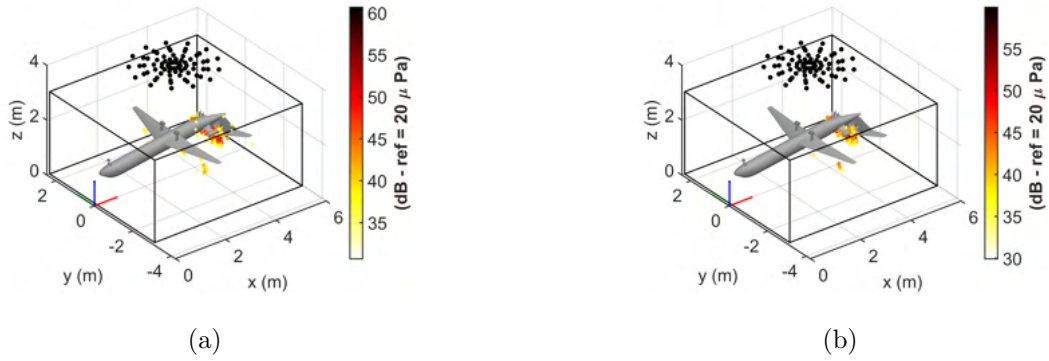

(a)

(b)

Figure 30: CROR turned-on. Top array and CLEAN-SC. (a) $\varphi = 1$, (b) $\varphi = 0.6$.
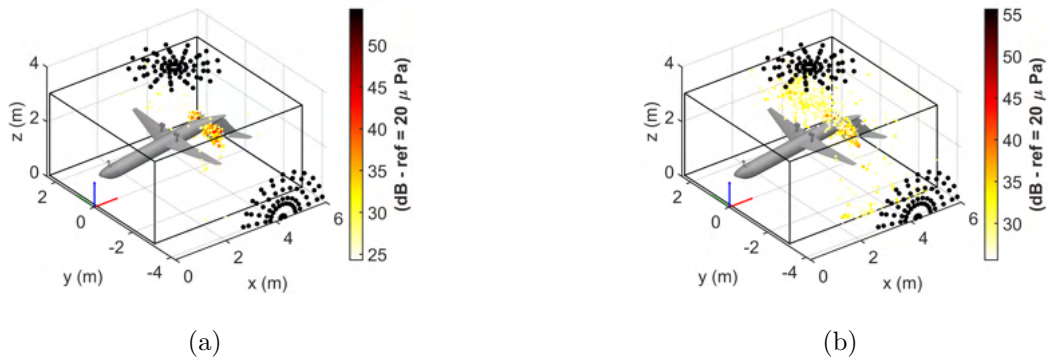

(a)

(b)

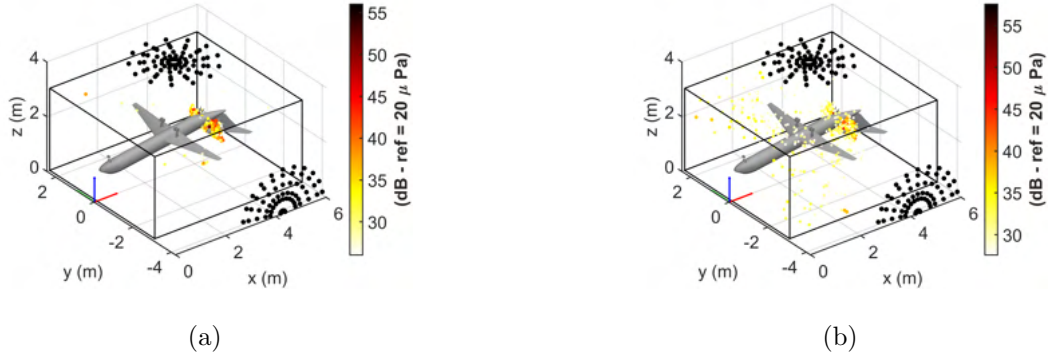Figure 31: CROR turned-on. Side and top arrays and ESM-IRLS. (a) CSCD, (b) ED.

(a)   (b)

Figure 32: CROR turned-on. Side and top arrays and ESM-IRLS with CB map as a priori information. (a) CSCD, (b) ED.

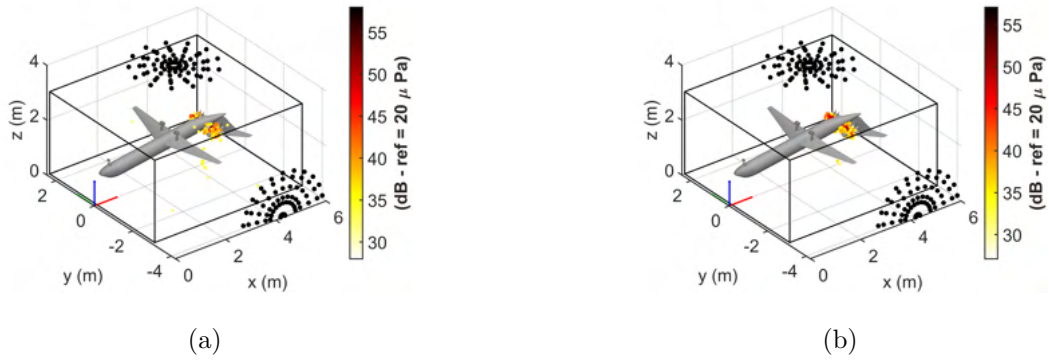(a)   (b)

Figure 33: CROR turned-on. Side and top arrays and CLEAN-SC. (a) $\varphi = 1$, (b) $\varphi = 0.6$.
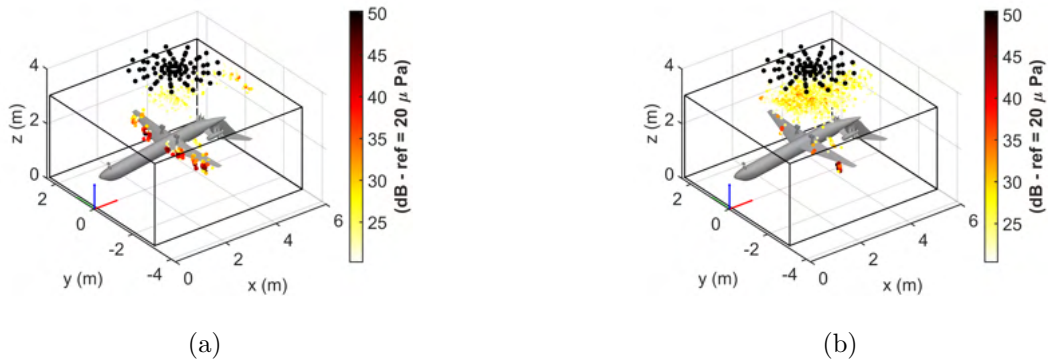

(a)   (b)

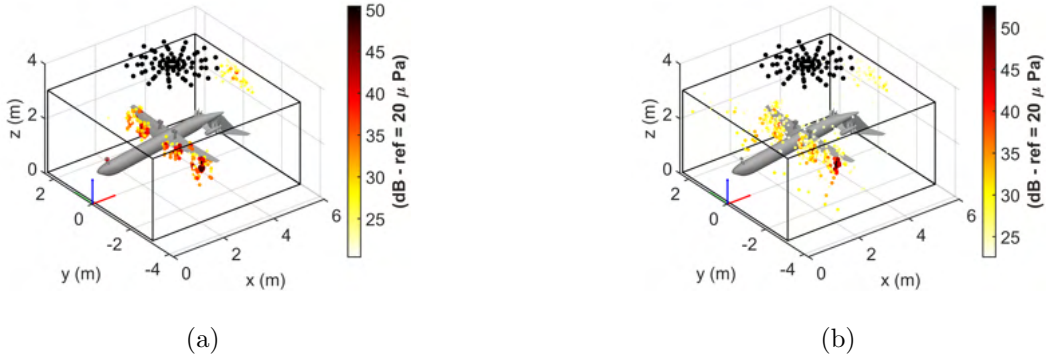Figure 34: CROR turned-off. Top array and ESM-IRLS. (a) CSCD, (b) ED.

Figure 35: CROR turned-off. Top array and ESM-IRLS with CB map as a priori information. (a) CSCD, (b) ED.
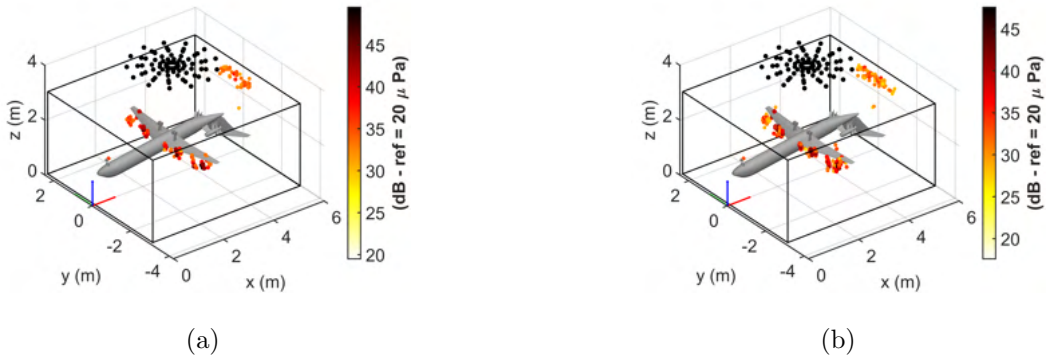

Figure 36: CROR turned-off. Top array and CLEAN-SC. (a) $\varphi = 1$, (b) $\varphi = 0.6$.
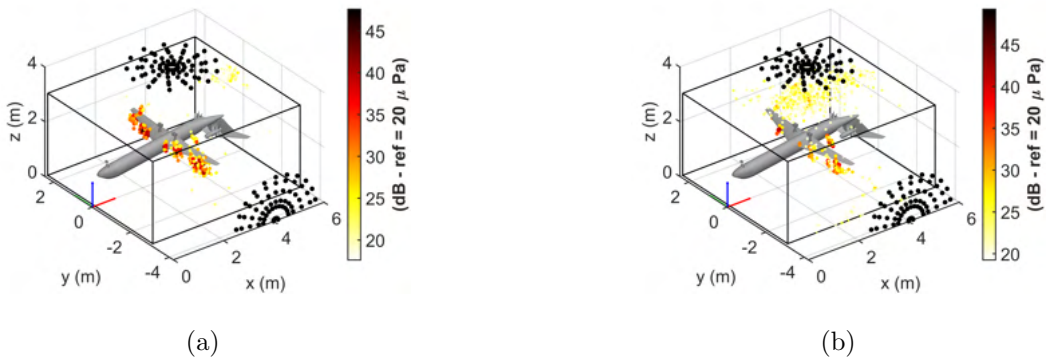

Figure 37: CROR turned-off. Side and top array and ESM-IRLS. (a) CSCD, (b) ED.
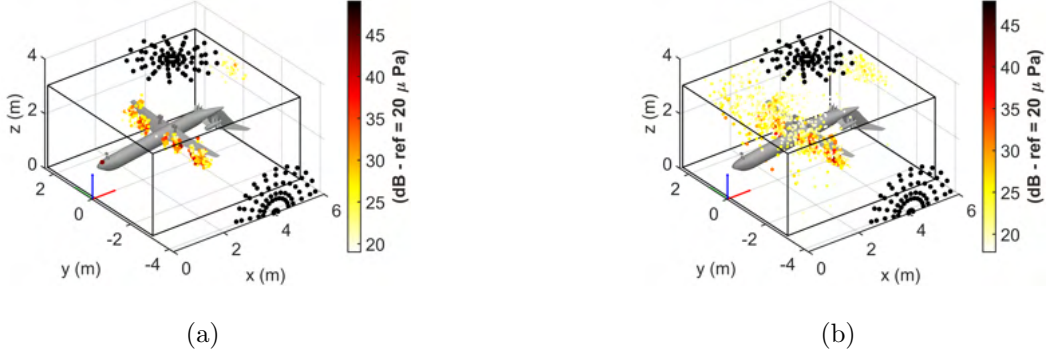
54

(a)   (b)

Figure 38: CROR turned-off. Side and top array and ESM-IRLS with CB map as a priori information. (a) CSCD, (b) ED.
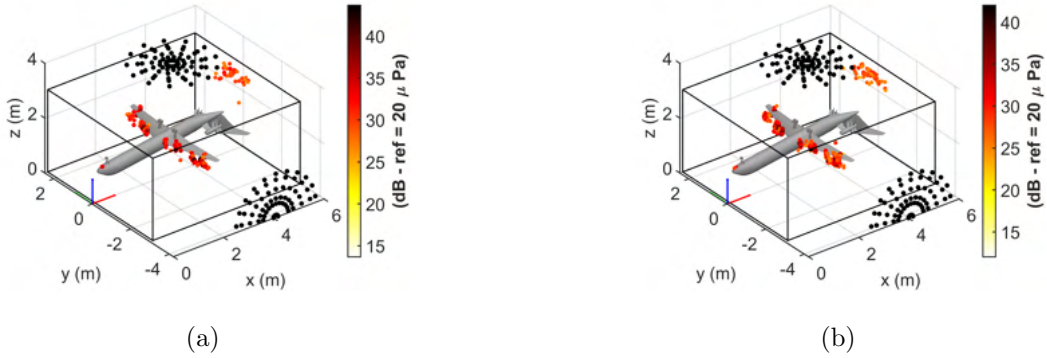

(a)   (b)

Figure 39: CROR turned-off. Side and top arrays and CLEAN-SC. (a) $\varphi = 1$, (b) $\varphi = 0.6$.

The maps obtained from experimental data are quite different depending on the method. The main reasons are analyzed here. Maps returned by CLEAN-SC are the most reliable and the dependence on loop gain is low. As mentioned above, a value of $\varphi < 1$ may reveal some more information of source extension, as it happens here. However, the maps obtained with ESM-IRLS return more complete maps than CLEAN-SC. Indeed, a part of these additional equivalent sources are related to artefacts due to the BGN and/or instabilities, but it is also noticeable the increase of the extension of

55

sources in the zones of CRORs or the leading-edge. Another important aspect to consider is that many solutions of inverse problem presents instabilities already mentioned about simulated experiments. It is possible to notice this especially when no a priori information is introduced and/or ED is adopted to decompose the CSM (Figures 28, 31(b), 34, 37(b)). Ill-posedness of the problem, high level of noise and bad source/noise separation are the main causes of this issue. In fact, introducing CB maps as a priori information this issues is avoided in this application. Results on experimental data clearly highlight the huge difference between ED and CSCD. In fact, even when instability of solution is avoided, maps obtained with ED are severely spoiled by noise (Figures 29, 35, 38). This difference is rooted in the fact that eigenmodes are a mixture of several contribution, while CSCD achieves better separation . Therefore, the latter better reflects the assumption of sparsity, thus making it possible better noise suppression and accuracy of localization.

In general, the main source of noise is always detected even in presence of low SNR. In fact, when CRORs are active, the aerodynamic noise is only slightly visible in the maps, while it clearly appears when the rotor are turned-off. The use of two arrays gives an improvement in the localization of rotors noise, while it brings no advantage in revealing aeroacoustic noise when the rotor is active. Indeed, only in Figure 29(a), some aeroacoustic sources are clearly visible in addition to the CROR sources. When CRORs are turned-off, some sources close to the wings, that might hint to wing tip noise, starts to appear on the maps, even if the background noise remains the same.

In this case the second array improves the compactness of localization of aeroacoustic sources.

Last aspect treated here is the calculation time needed for volumetric mapping of these test cases with ESM-IRLS. Since it is an inverse method, calculation time is strongly dependant on the settings and the content of data. Therefore, only some general considerations are provided here. The average calculation time per each frequency line of all calculations presented in this section about experimental data is 0.152 hours, while the minimum is 0.064 hours and the maximum is 0.282 hours. The worst case is with the dual array, ED and no a priori information. In fact, the latter better addresses the problem and speeds up the discard of potential sources. While CSCD automatically returns the number of relevant components, thus reducing the number of components to map. In addition, the better source separation achieved by CSCD enhances the reduction of computation time needed with respect to ED. Obviously, the lower is number of microphones the lower is the computation demand. Computation demand of CLEAN-SC is clearly much smaller than ESM-IRLS, thus making it the best candidate for a "first attempt map" to better set the inverse problem.

6. Conclusions

This work described how to exploit inverse methods in the context of volumetric mapping targeted to aeroacoustic applications. Firstly, the analysis of volumetric mapping problems is discussed, noticing that some well-known issues of acoustic imaging are strongly enhanced in these applications. An inverse method, named ESM-IRLS, has been formulated, presenting step-by-step the assumptions and the strategies at its basis. The inverse method presented here aims at returning a sparse approximation of the source field making use of Iterative Reweighted Least-Squares and Bayesian Regularization. The choice of these two fulfils the requirements of sparsity constraint and reliable regularization. However, other strategies must be adopted for volumetric imaging. The issue of balancing the energy among potential sources has been addressed, adopting the proper formulation of acoustic propagator. Also some algorithmic strategies have been implemented to make the method faster and more accurate, such as a thresholding step and a robust convergence criterion. It has also been demonstrated that the introduction of a priori information hugely improves localization and quantification abilities, especially in presence of strong background noise. Genrerally, input of acoustic imaging method is the Cross-Spectral-Matrix of microphone array. A novel approach proposed in this paper makes the use of CLEAN-SC as decomposition tool of CSM. Similarly to classic Eigenmode Decomposition, this tool is able to extract coherent source components from CSM. These can be used to set separate inverse problems and retrieve the full map from the energetic sum of maps of all components. This approach gives two advantages: lower amount of noise is present in data used to set the problem and

58

the assumption of sparsity can be better fulfilled. The CLEAN-SC decomposition has been combined with ESM-IRLS. On the other hand, ESM-IRLS has been combined also with the standard ED, showing that the latter is outperformed by the approach based on CSCD, especially with experimental aeroacoustic data. On the one hand, the same method has been compared with the standard CLEAN-SC deconvolution approach. Despite the robustness of maps returned by CLEAN-SC, ESM-IRLS combined with the CSCD is able to reveal much more spatial information about spatially extended or coherent sources.

Results from both simulated and experimental data demonstrated that is possible to use a single planar array to map aeroacoustic noise sources with fair accuracy. The use of a second array is suggested when localization accuracy is crucial. However, the downside of combining multiple arrays looking at the acoustic scene from different point of view, is that one of them may not detect enough signal from some sources acting in the scenario (e.g. due to masking effect of the target object or excessive source directivity) thus deteriorating the reconstruction of these sources. Moreover, the introduction of CB map for each component as a priori information in the inverse problem makes it possible to correctly reconstruct even sources 20 dB weaker than the strongest one. Source quantification is accurate especially for the main source, but the reconstructed level suffers of slightly underestimation. As the background noise level increases the error in reconstructed spectra becomes more relevant. Independently on the use of one or two arrays, results showed that the algorithm and the strategies described in this work can lead to accu-

rate volumetric source localization and good quantification even in presence of strong background noise.

Acknowledgements

References

[1] P. Chiariotti, M. Martarelli, P. Castellini, Acoustic beamforming for noise source localization – reviews, methodology and applications, Mechanical Systems and Signal Processing 120 (2019) 422–448. doi:`10.1016/j.ymssp.2018.09.019`.

[2] M. Legg, S. Bradley, Automatic 3d scanning surface generation for microphone array acoustic imaging, Applied Acoustics 76 (2014) 230–237. doi:`10.1016/j.apacoust.2013.08.008`.

[3] P. Chiariotti, G. Battista, M. Ettorre, P. Castellini, Average acoustic beamforming in car cabins: An automatic system for acoustic mapping over 3d surfaces, Applied Acoustics 129 (2018) 47 – 63. URL: `http://www.sciencedirect.com/science/article/pii/S0003682X17306618`. doi:`https://doi.org/10.1016/j.apacoust.2017.07.009`.

60

[4] D. Döbler, J. Ocker, C. Puhle, On 3D-beamforming in the wind tunnel, 2016.

[5] T. F. Brooks, W. M. Humphreys, Jr, A Deconvolution Approach for the Mapping of Acoustic Sources (DAMAS) Determined from Phased Microphone Arrays, in: 10th AIAA/CEAS Aeroacoustics Conference, 2004.

[6] P. Sijtsma, Clean based on spatial source coherence, International Journal of Aeroacoustics 6 (2007) 357–374. URL: http://dx.doi.org/10.1260/147547207783359459.

[7] E. Sarradj, Three-dimensional acoustic source mapping with different beamforming steering vector formulations, Advances in Acoustics and Vibration 2012 (2012) 1–12. doi:10.1155/2012/292695.

[8] T. F. Brooks, W. M. Humphreys, Jr, Three-Dimensional Applications of DAMAS Methodology for Aeroacoustic Noise Source Definition, in: 11th AIAA/CEAS Aeroacoustics Conference, Monterey, California, May 23-25, 2005, 2005.

[9] R. Porteous, Z. Prime, C. Doolan, D. Moreau, V. Valeau, Three-dimensional beamforming of dipolar aeroacoustic sources, Journal of Sound and Vibration 355 (2015) 117–134. doi:10.1016/j.jsv.2015.06.030.

[10] T. Padois, A. Berry, Two and three-dimensional sound source localization with beamforming and several deconvolution techniques, Acta

Acustica united with Acustica 103 (2017) 392–400. doi:10.3813/aaa.919069.

[11] G. Battista, P. Chiariotti, G. Herold, E. Sarradj, P. Castellini, Inverse methods for three-dimensional acoustic mapping with a single planar array, in: Proceedings of the 7th Berlin Beamforming Conference, 2018.

[12] F. Ning, J. Wei, L. Qiu, H. Shi, X. Li, Three-dimensional acoustic imaging with planar microphone arrays and compressive sensing, Journal of Sound and Vibration 380 (2016) 112–128. doi:10.1016/j.jsv.2016.06.009.

[13] G. H. Koopmann, L. Song, J. B. Fahnline, A method for computing acoustic fields based on the principle of wave superposition, The Journal of the Acoustical Society of America 86 (1989) 2433–2438. doi:10.1121/1.398450.

[14] J. Hadamard, Sur les problèmes aux dérivés partielles et leur signification physique,(On the partial derivative problems and their physical meaning), Princeton University Bulletin 13 (1902) 49–52.

[15] Q. Leclère, A. Pereira, C. Bailly, J. Antoni, C. Picard, A unified formalism for acoustic imaging based on microphone array measurements, International Journal of Aeroacoustics 16 (2017) 431–456. doi:10.1177/1475472x17718883.

[16] A. Pereira, Acoustic imaging in enclosed spaces, Ph.D. thesis, INSA de Lyon, 2014.

62

[17] T. Suzuki, L1 generalized inverse beam-forming algorithm resolving coherent/incoherent, distributed and multipole sources, Journal of Sound and Vibration 330 (2011) 5835–5851. doi:10.1016/j.jsv.2011.05.021.

[18] A. N. Tikhonov, Solution of incorrectly formulated problems and the regularization method, Soviet Math. Dokl. 4 (1963) 1035–1038.

[19] J. Antoni, A bayesian approach to sound source reconstruction: Optimal basis, regularization, and focusing, The Journal of the Acoustical Society of America 131 (2012) 2873–2890. doi:10.1121/1.3685484.

[20] S. Mallat, Z. Zhang, Matching pursuits with time-frequency dictionaries, IEEE Transactions on Signal Processing 41 (1993) 3397–3415. doi:10.1109/78.258082.

[21] Y. Pati, R. Rezaiifar, P. Krishnaprasad, Orthogonal matching pursuit: recursive function approximation with applications to wavelet decomposition, in: Proceedings of 27th Asilomar Conference on Signals, Systems and Computers, IEEE Comput. Soc. Press, ???? doi:10.1109/acssc.1993.342465.

[22] S. Bourguignon, J. Ninin, H. Carfantan, M. Mongeau, Exact sparse approximation problems via mixed-integer programming: Formulations and computational performance, IEEE Transactions on Signal Processing 64 (2016) 1405–1419. doi:10.1109/tsp.2015.2496367.

[23] P. R. Gill, A. Wang, A. Molnar, The in-crowd algorithm for fast basis pursuit denoising, IEEE Transactions on Signal Processing 59 (2011) 4595–4605. doi:10.1109/tsp.2011.2161292.

63

[24] R. Tibshirani, Regression shrinkage and selection via the lasso: a retrospective, Journal of the Royal Statistical Society: Series B (Statistical Methodology) 73 (2011) 273–282. doi:`10.1111/j.1467-9868.2011.00771.x`.

[25] R. Chartrand, W. Yin, Iteratively reweighted algorithms for compressive sensing, in: 2008 IEEE International Conference on Acoustics, Speech and Signal Processing, IEEE, 2008. doi:`10.1109/icassp.2008.4518498`.

[26] Q. Leclere, A. Pereira, J. Antoni, Une approche bayésienne de la parcimonie pour l'identification de sources acoustiques (A Bayesian approach for sparse acoustic source identification), in: Congrès Français d'Acoustique, Poitiers, France, 2014, pp. –. URL: `https://hal.archives-ouvertes.fr/hal-01006192`.

[27] Q. Leclère, Acoustic imaging using under-determined inverse approaches: Frequency limitations and optimal regularization, Journal of Sound and Vibration 321 (2009) 605–619. doi:`10.1016/j.jsv.2008.10.022`.

[28] A. Pereira, J. Antoni, Q. Leclère, Empirical bayesian regularization of the inverse acoustic problem, Applied Acoustics 97 (2015) 11–29. doi:`10.1016/j.apacoust.2015.03.008`.

[29] F. Champagnat, J. Idier, A connection between half-quadratic criteria and EM algorithms, IEEE Signal Processing Letters 11 (2004) 709–712. doi:`10.1109/lsp.2004.833511`.

[30] B. Oudompheng, A. Pereira, C. Picard, Q. Leclère, B. Nicolas, A theoretical and experimental comparison of the iterative equivalent source method and the generalized inverse beamforming, in: 5th BeBec, 2014. URL: `http://bebec.eu/Downloads/BeBeC2014/Papers/BeBeC-2014-12.pdf`.

[31] T. Padois, P.-A. Gauthier, A. Berry, Inverse problem with beamforming regularization matrix applied to sound source localization in closed wind-tunnel using microphone array, Journal of Sound and Vibration 333 (2014) 6858–6868.

[32] J. Antoni, T. L. Magueresse, Q. Leclère, P. Simard, Sparse acoustical holography from iterated bayesian focusing, Journal of Sound and Vibration 446 (2019) 289–325. doi:`10.1016/j.jsv.2019.01.001`.

[33] T. Yardibi, J. Li, P. Stoica, L. N. Cattafesta, Sparsity constrained deconvolution approaches for acoustic source mapping, The Journal of the Acoustical Society of America 123 (2008) 2631–2642. URL: `http://scitation.aip.org/content/asa/journal/jasa/123/5/10.1121/1.2896754`. doi:`http://dx.doi.org/10.1121/1.2896754`.

[34] B. Dong, J. Antoni, E. Zhang, Blind separation of sound sources from the principle of least spatial entropy, Journal of Sound and Vibration 333 (2014) 2643–2668.

[35] E. Sarradj, C. Schulze, A. Zeibig, Identification of noise source mechanisms using orthogonal beamforming, Noise and Vibration: Emerging Methods (2005).

[36] S. Oerlemans, P. Sijtsma, Determination of Absolute Levels from Phased Array Measurements Using Spatial Source Coherence, in: 8th AIAA/CEAS Aeroacoustics Conference and Exhibit, Breckenridge, Colorado, June 17-19, 2002, 2002.

[37] E. Sarradj, Three-dimensional acoustic source mapping, in: 4th Bebec, 2012.

[38] S. Luesutthiviboon, A. M. Malgoezar, R. Merino-Martinez, M. Snellen, P. Sijtsma, D. G. Simons, Enhanced HR-CLEAN-SC for resolving multiple closely spaced sound sources, International Journal of Aeroacoustics 18 (2019) 392–413. doi:10.1177/1475472x19852938.

[39] R. K. Amiet, Correction of open jet wind tunnel measurements for shear layer refraction, AIAA Journal (1975).

[40] A. Lauterbach, K. Ehrenfried, Procedure for the Accurate Phase Calibration of a Microphone Array, in: 15th AIAA/CEAS Aeroacoustics Conference, 2009. URL: http://pdf.aiaa.org/preview/CDReadyMAERO09_2131/PV2009_3122.pdf. doi:10.2514/6.2009-3122.

[41] M. Mosher, M. E. Watts, S. Jovic, S. M. Jaeger, Calibration of microphone arrays for phased array processing, in: 3rd AIAA/CEAS Aeroacoustics Conference, 1997. URL: http://pdf.aiaa.org/preview/1997/PV1997_1678.pdf.